J. Fluid Mech. (2023), *vol*. 957, A11, doi:10.1017/jfm.2023.51

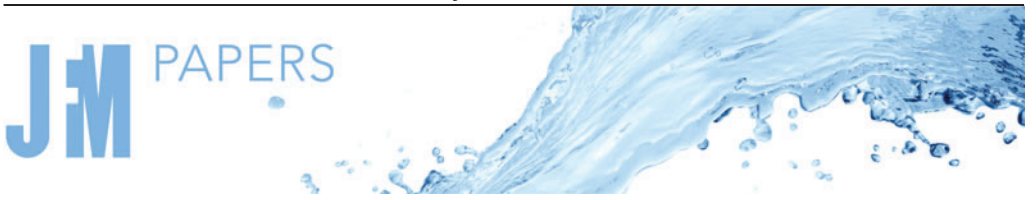

Spatio-temporal dynamics of a two-layer pressure-driven flow subjected to a wall-normal temperature gradient

Ramkarn Patne[1],† **and Jaikishan Chandarana**[1]

[1]Department of Chemical Engineering, Indian Institute of Technology Hyderabad, Kandi, Sangareddy 502285, India

(Received 30 August 2022; revised 2 January 2023; accepted 10 January 2023)

The present study investigates the linear spatio-temporal and weakly nonlinear stability of a pressure-driven two-layer channel flow subjected to a wall-normal temperature gradient commonly encountered in industrial applications. The liquid–liquid interface tension is assumed to be a linearly decreasing function of temperature. The study employs both numerical (pseudo-spectral method) and long-wave approaches. The general linear stability analysis (GLSA) predicts shear-flow and thermocapillary modes that arise due to the imposed pressure and temperature gradients, respectively. The previous stability analyses of the same problem predicted a negligible effect of the pressure-driven flow on the linear stability of the system. However, the GLSA reveals stabilising and destabilising effects of the pressure-driven flow depending on the viscosity ratio (μ_r), thermal conductivity ratio (κ_r), interface position (H) and the sign of the imposed temperature gradient (β_1). The analysis predicts a range of H for given μ_r and κ_r, which can not be stabilised by the thermocapillarity. The numerically predicted long-wave instability is then captured using the long-wave asymptotic approach. The arguments based on the physical mechanism further successfully explain the role of μ_r, κ_r, H, the sign of β_1 and the interaction between the velocity and temperature perturbations in stabilising/destabilising the flow. The spatio-temporal analysis reveals the dominance of the spanwise mode in causing the absolutely unstable flow. The weakly nonlinear analysis reveals a subcritical pitchfork bifurcation without shear flow. However, with the shear flow, the streamwise mode undergoes a supercritical Hopf bifurcation.

Key words: multiphase flow, Marangoni convection

† Email address for correspondence: ramkarn@che.iith.ac.in

1. Introduction

Multi-layer channel flows subjected to a temperature gradient are encountered in polymer processing (Joseph & Renardy 1993; Joseph *et al.* 1997), microfluidic applications involving large bubbles (Bretherton 1961; Alvarez & Uguz 2013), additive manufacturing (Gibson, Rosen & Stucker 2010), material processing and crystal growth (Lappa 2010), reactive flows (Levenspiel 1999) and industrial processes such as coating and drying (Kistler & Schweizer 1997). For example, in the fused-filament-fabrication additive manufacturing process, a product comprised of a polymer composite can be obtained using a layered feed of required polymer filaments (Quan *et al.* 2015; Chua & Leong 2017; Goh *et al.* 2018; Rajak *et al.* 2019). The fed filaments are then heated to obtain a multi-layered flow of the molten polymers that then exits through the nozzle and is deposited on a substrate to obtain the desired product. This system can be modelled as a multi-layer pressure-driven polymer flow subjected to a wall-normal temperature gradient. The present study could also be relevant in manipulating the mixing in multi-layered microfluidic flows wherein the wall-normal temperature gradient could be utilised as a controlling parameter to enhance or reduce the mixing of the fluids. To understand the role of the liquid–liquid interface in determining the dynamics of the system, here we consider a two-layer pressure-driven flow. The multi-layered flows could exhibit various instabilities due to the shear-flow and temperature dependence of the physical properties of the fluids. The present study aims to investigate the shear-flow and thermocapillary instabilities. The thermocapillary instability arises from the temperature dependence of the interface tension and an ensuing emergence of shear stress at the interface (Pearson 1958; Oron, Davis & Bankoff 1997). While the shear-flow instabilities arise due to the viscosity stratification (Yih 1967), which leads to the development of longitudinal velocity perturbations.

For a liquid layer supported by a heated substrate and a free surface, thermocapillary instabilities exist as the Marangoni number crosses a threshold or critical value Ma_c. As explained in the literature (Smith & Davis 1983*a*,*b*; Patne *et al.* 2022), for such a system to exhibit a thermocapillary instability, the free surface temperature of the liquid must be lower than that of the substrate. Here, we have a two-layer system with plate 1 at $y^* = 0$ maintained at temperature T_1^* and plate 2 at $y^* = R$ maintained at temperature T_2^*, where the asterisk implies a dimensional quantity. First, consider the case when $T_1^* < T_2^*$ for which fluid 1 will have the interface temperature higher than the temperature at $y^* = 0$, thus (following the above arguments), it will have a stabilising effect on the thermocapillary mode. However, for fluid 2, the interface will be at a lower temperature compared with the plate at $y^* = R$. Thus, it will have a destabilising effect on the thermocapillary mode. The opposite is the case when $T_1^* > T_2^*$. Additionally, the viscosity stratification leads to a shear-flow instability, which may interact with the thermocapillary mode via the tangential stress balance condition at the interface. Thus, there is a competition between the stabilising and destabilising influence of the fluid layers to manifest thermocapillary and shear-flow instabilities. The above considerations lead to the following questions. How do the shear-flow and thermocapillary modes interact? Do the physical properties of the fluids, *viz.*, viscosity and thermal conductivity, interface position and the sign of the imposed temperature gradient, affect the stability of the flow? How can one explain the physical mechanism (similar to a single layer) by which the flow will become unstable? The present study aims to answer these questions.

Yih (1967) predicted shear-flow instability in a two-layer isothermal Couette–Poiseuille flow and ascribed the unstable mode to the viscosity stratification. From his study, the shear-flow instability could exist in a viscosity-stratified multi-layer flow, provided that

finite inertia and a deformable liquid–liquid interface exist. Yiantsios & Higgins (1988) extended his study to include the short-wave instability and the presence of the density and thickness ratios. They also carried out an asymptotic analysis to capture the short-wave instability. Tilley, Davis & Bankoff (1994) considered a similar problem in an inclined channel for specific cases of air–water and olive oil–water for an arbitrary wavenumber. Barmak *et al.* (1994) studied the same problem for an arbitrary wavenumber using the Chebyshev collocation method and predicted that there is no definite correlation between the type of instability and the perturbation wavelength.

Georis *et al.* (1993, 1999), Madruga, Pérez-Garcia & Lebon (2003), Nepomnyashchy & Simanovskii (2006), Madruga, Pérez-Garcia & Lebon (2004) and Simanovskii (2007) investigated the dynamics of the multi-layer system subjected to a wall-normal temperature gradient in the absence of an imposed temperature gradient and assumed a non-deformable interface thereby missing the main ingredient, i.e. interface deformability and absence of the base flow, necessary for the existence of the shear-flow instability. However, they could predict thermocapillary instability at a higher Marangoni number. The deformability of the interface and the presence of the shear flow were considered by Alvarez & Uguz (2013) for a three-layer Poiseuille flow subjected to a wall-normal temperature gradient. However, their analysis was focused on the case with no shear flow, i.e. the absence of the applied pressure gradient, thus, they did not present results for the critical Marangoni number when the shear flow was present. Furthermore, they predicted a negligible effect of the applied pressure gradient on the growth rate (i.e. stability) while the present study clearly shows (using analytical and numerical calculations and physical arguments) that the applied pressure gradient can have both stabilising and destabilising effects depending on the parameters.

Wei (2006) analysed the stability of a two-layer Couette flow with a deformable interface under an imposed temperature gradient across the bounding plates with the linear dependence of the interface tension on the temperature. He assumed one fluid layer in the thin-film limit to proceed with the long-wave asymptotic analysis and governing equation derivation. The thin-film equations showed the presence of a non-local term that played an important role in determining the competition between the inertial and thermocapillary forces. His study showed an interesting interplay between the shear-flow and thermocapillary instabilities.

The analysis of Wei (2006) was focused on predicting the existence of the instability but lacked an explanation regarding the physical mechanism of the instabilities, thereby leaving an important gap in the understanding of the dynamics of the flows. Also, Wei (2006) studied a two-layer Couette flow whose stability characteristics widely differ from those of practically important pressure-driven two-layer channel flows. Furthermore, Wei (2006) considered only temporal dynamics of the flows, which may be inadequate in the applications. For example, in the co-extrusion of polymers in the presence of the temperature gradient relevant in the fused-filament-fabrication (Gibson *et al.* 2010) and polymer processing (Bird, Armstrong & Hassager 1977), only spatio-temporal analysis can determine the existence of the detrimental absolute instability, thereby necessitating the spatio-temporal analysis.

The spatio-temporal instability can be further classified as absolute or convective instabilities. Absolute instability implies the growth of disturbances at a fixed point in space while convective instability implies that, given sufficient time, the disturbances will decay at a fixed point in space. The present study aims to address the shortcomings of the previous studies by analysing in detail the linear spatio-temporal dynamics of a two-layer pressure-driven channel flow. It must be noted that Sahu & Matar (2011) studied

the spatio-temporal dynamics of the two-layer isothermal Poiseuille flow and predicted the existence of the absolute instability, provided that the Reynolds number is sufficiently high. The present study augments their study by including the effect of the wall-normal temperature gradient and shows that the flow can exhibit absolute instability at a much lower Reynolds number. Also, unlike Wei (2006), here we do not assume long-wave disturbances, instead a general linear stability analysis (GLSA) applicable for the whole wavenumber range is carried out. To analytically capture the numerically predicted instability, a long-wave asymptotic analysis is carried out. The weakly nonlinear stability analysis carried out in the present study also shows the impact of the pressure-driven flow on the type of bifurcation the two-layer system will undergo.

The rest of the paper is arranged as follows. The base-state and linearised perturbation governing equations are derived in § 2. The numerical method utilised to carry out the GLSA is briefly explained in § 3. The results obtained by GLSA and long-wave asymptotic analysis to capture the modes predicted by the GLSA are presented in § 4. The physical mechanism of the thermocapillary and shear-flow modes and their interplay is discussed in § 5. The long-wave equation derivation, linear spatio-temporal analysis and weakly nonlinear stability analysis are discussed in § 6. The salient conclusions of the current study are presented in § 7.

2. Problem formulation

Two immiscible and incompressible Newtonian fluids flowing in a channel, extending from 0 to R in the y direction, with the interface located at $y^* = HR$ are subjected to a temperature gradient along the y axis. The fluids are assumed to extend infinitely in the lateral direction (along the z axis). The plates at $y^* = 0$ and $y^* = R$ are maintained at temperatures T_1^* and T_2^*, respectively, such that $T_1^* \neq T_2^*$, thereby imposing a temperature gradient across the fluid layers. The two fluids, marked as 1 and 2, have different viscosities μ_1 and μ_2 and thermal conductivities κ_1 and κ_2, respectively, but equal heat capacity c_p and density ρ.

The liquid–liquid interface tension, σ, is assumed to be linearly temperature dependent,

$$\sigma^* = \sigma_0 - \gamma(T_i^* - T_0^*), \tag{2.1}$$

where T_i^* is the local interface temperature, $\gamma = -\mathrm{d}\sigma^*/\mathrm{d}T^* > 0$, and σ_0 is the interface tension of the fluid at the reference temperature T_0^*. This feature results in the emergence of Marangoni stresses at the interface.

The Cartesian reference frame chosen here contains the x and z axes located in the lower wall and the y axis normal to the latter and directed into the two-layer system. The lengths in the present problem are scaled by the channel spacing, R. The components of the velocity field are scaled by the interface velocity V_I, pressure by $\mu V_I/R$, temperature by βHR and the time t is scaled by R/V_I, where $\beta = \mathrm{d}\bar{T}^{(1)*}/\mathrm{d}y^*$ is the base-state temperature gradient across fluid 1. In the dimensionless coordinates, fluids 1 and 2 are confined to the domains $[0, H]$ and $[H, 1]$, respectively. The schematic of the flow geometry under consideration is shown in figure 1.

The velocity fields in the two fluids are $\boldsymbol{v}^{(i)} = (v_x^{(i)}, v_y^{(i)}, v_z^{(i)})$, where $i = 1, 2$ represent fluids 1 and 2, respectively. The dimensionless continuity equation is

$$\boldsymbol{\nabla} \cdot \boldsymbol{v}^{(i)} = 0, \tag{2.2a}$$

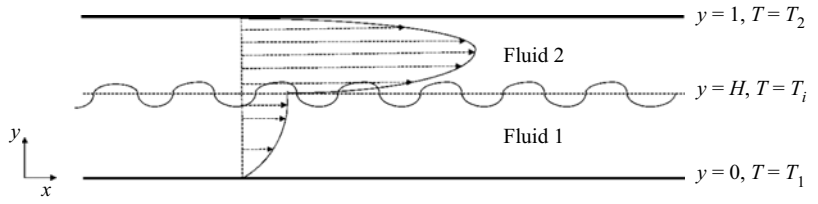

Figure 1. Schematic of a two-layer plane Poiseuille flow subjected to a wall-normal temperature gradient in scaled quantities. The velocity profile is shown for $\mu_1 > \mu_2$. For $T_1 \neq T_2$, thermocapillary stresses develop along the interface due to the temperature dependence of the interface tension.

where the gradient operator is $\boldsymbol{\nabla} = \boldsymbol{e}_x\partial_x + \boldsymbol{e}_y\partial_y + \boldsymbol{e}_z\partial_z$, with $\boldsymbol{e}_j$ denoting the unit vector in the j direction. The dimensionless Navier–Stokes equations for the fluids are

$$Re[\partial_t \boldsymbol{v}^{(i)} + (\boldsymbol{v}^{(i)} \cdot \boldsymbol{\nabla})\boldsymbol{v}^{(i)}] = -\boldsymbol{\nabla} p^{(i)} + \mu^{(i)}\nabla^2 \boldsymbol{v}^{(i)}, \tag{2.2b}$$

in which $Re \equiv \rho V_I R/\mu_1$ is the Reynolds number and $\nabla^2 \equiv \partial_x^2 + \partial_y^2 + \partial_z^2$ is the Laplacian operator. The dimensionless viscosities are $\mu^{(1)} = 1$ for fluid 1 and $\mu^{(2)} = \mu_r \equiv \mu_2/\mu_1$ for fluid 2. The dimensionless energy equations are

$$Re\, Pr[\partial_t T^{(i)} + (\boldsymbol{v}^{(i)} \cdot \boldsymbol{\nabla})T^{(i)}] = \kappa^{(i)}\nabla^2 T^{(i)}, \tag{2.2c}$$

where $Pr = \mu_1 c_p/\kappa_1$ is the Prandtl number based on the properties of fluid 1. The dimensionless thermal conductivities are $\kappa^{(1)} = 1$ for fluid 1 and $\kappa^{(2)} = \kappa_r \equiv \kappa_2/\kappa_1$ for fluid 2.

The governing equations (2.2) are subjected to the following boundary conditions. Assuming no-slip, impermeable plates and fixed temperatures at the bounding plates yield

$$v_x^{(1)} = 0; \quad v_y^{(1)} = 0; \quad v_z^{(1)} = 0; \quad T^{(1)} = T_1, \quad \text{at } y = 0, \tag{2.3a}$$

$$v_x^{(2)} = 0; \quad v_y^{(2)} = 0; \quad v_z^{(2)} = 0; \quad T^{(2)} = T_2, \quad \text{at } y = 1. \tag{2.3b}$$

For the linear stability analysis, the assumption of two-dimensional disturbances is not applicable for the present system due to the thermocapillarity, which can excite spanwise unstable modes earlier than the streamwise modes implying inapplicability of the Squire's theorem (Pearson 1958). Thus, henceforth three-dimensional disturbances will be considered for the stability analysis. The fluid–fluid interface is located at $y = H + \xi(x, t)$, where $\xi(x, t)$ is the infinitesimal displacement of the interface from its undisturbed position, $y = H$. The boundary conditions at the interface are the kinematic boundary condition, the balance of the tangential and normal components of the velocities and stresses, as well as the balance of the temperature and heat flux, as follows:

$$\partial_t \xi + v_x \partial_x \xi = v_y, \tag{2.3c}$$

$$\boldsymbol{v}^{(1)} - \boldsymbol{v}^{(2)} = 0, \tag{2.3d}$$

$$\boldsymbol{t_1} \cdot \boldsymbol{\tau}^{(1)} \cdot \boldsymbol{n} - \boldsymbol{t_1} \cdot \boldsymbol{\tau}^{(2)} \cdot \boldsymbol{n} = -Ma\boldsymbol{\nabla} T \cdot \boldsymbol{t_1}, \tag{2.3e}$$

$$\boldsymbol{t_2} \cdot \boldsymbol{\tau}^{(1)} \cdot \boldsymbol{n} - \boldsymbol{t_2} \cdot \boldsymbol{\tau}^{(2)} \cdot \boldsymbol{n} = -Ma\boldsymbol{\nabla} T \cdot \boldsymbol{t_2}, \tag{2.3f}$$

$$-p^{(1)} + \boldsymbol{n} \cdot \boldsymbol{\tau}^{(1)} \cdot \boldsymbol{n} - (-p^{(2)} + \boldsymbol{n} \cdot \boldsymbol{\tau}^{(2)} \cdot \boldsymbol{n}) = -Ca^{-1}(\boldsymbol{\nabla} \cdot \boldsymbol{n}), \tag{2.3g}$$

$$T^{(1)} - T^{(2)} = 0, \tag{2.3h}$$

$$\boldsymbol{\nabla} T^{(1)} \cdot \boldsymbol{n} - \kappa_r \boldsymbol{\nabla} T^{(2)} \cdot \boldsymbol{n} = 0. \tag{2.3i}$$

Here $Ca = \mu_1 V_I/\sigma_0$ is the capillary number and $Ma = \gamma\beta HR/\mu_1 V_I$ is the Marangoni number. By definition, the sign of Ma is the same as that of the base-state temperature gradient across fluid 1, i.e. β. The Marangoni number can be rearranged as

$$Ma = \frac{\gamma\beta}{\mu_1 V_I/(HR)} = \frac{\text{Thermocapillary stress at the interface due to fluid 1}}{\text{Viscous stress at the interface due to fluid 1}}. \tag{2.4}$$

Thus, the Marangoni number defined here gives relative importance of the thermocapillary and viscous stresses due to fluid 1 along the interface.

The vectors $\boldsymbol{t_1}$, $\boldsymbol{t_2}$ and $\boldsymbol{n}$ represent the unit tangent and normal vectors to the free surface, respectively. The linearised expressions for the normal and tangential vectors at the free surface in the perturbed state are

$$\boldsymbol{n} = -\partial_x\xi\boldsymbol{e_x} + \boldsymbol{e_y} - \partial_z\xi\boldsymbol{e_z}; \quad \boldsymbol{t_1} = \boldsymbol{e_x} + \partial_x\xi\boldsymbol{e_y}; \quad \boldsymbol{t_2} = \boldsymbol{e_z} + \partial_z\xi\boldsymbol{e_y}. \tag{2.5a–c}$$

2.1. *Base state*

A steady-state, fully developed pressure-driven bilayer flow has base-state velocities

$$\bar{v}_x^{(1)} = \frac{y[y - 1 - H(\mu_r - 1)(H - y)]}{(H - 1)H}, \tag{2.6a}$$

$$\bar{v}_x^{(2)} = \frac{(y - 1)[y - H(\mu_r - 1)(H - 1 - y)]}{(H - 1)H\mu_r}. \tag{2.6b}$$

Similarly, the base-state temperature gradients are

$$\frac{\partial\bar{T}^{(1)}}{\partial y} = 1; \quad \frac{\partial\bar{T}^{(2)}}{\partial y} = \frac{1}{\kappa_r}, \tag{2.6c}$$

$$\beta_1 = \frac{\kappa_2(T_2^* - T_1^*)}{[(1 - H)\kappa_1 + H\kappa_2]R}. \tag{2.6d}$$

The subsequent linear stability analysis is performed with respect to this base state.

2.2. *Linearised perturbation equations*

For the linear stability analysis, dynamical quantities such as velocities, temperatures and pressures are decomposed into the base-state and perturbed state, as $\mathcal{F}(\boldsymbol{x}, t) = \bar{\mathcal{F}}(y) + \mathcal{F}'(\boldsymbol{x}, t)$. Here, $\mathcal{F}(\boldsymbol{x}, t)$ is any dynamic quantity and a prime signifies the small perturbation quantity. In the linearised governing equations, the normal modes of the following form are then substituted:

$$\mathcal{F}'(\boldsymbol{x}, t) = \tilde{\mathcal{F}}(y)\exp(\mathrm{i}(kx + mz - \omega t)). \tag{2.7}$$

Here k and m are the wavenumbers and $\tilde{\mathcal{F}}(y)$ is the eigenfunction of $\mathcal{F}'(\boldsymbol{x}, t)$. The other parameter, $\omega = \omega_r + \mathrm{i}\omega_i$, is the complex frequency, which characterises the temporal phase speed and growth of the disturbances. For the temporal stability analysis, the wavenumbers are treated as real numbers, while for the spatio-temporal analysis, the wavenumbers are complex numbers. The flow is considered temporally unstable if at least one eigenvalue satisfies the condition $\omega_i > 0$. As described in § 6.2, the flow is absolutely unstable if the imaginary part of the complex frequency at the cusp point (ω_{i0}) satisfies the

condition $\omega_{i0} > 0$, otherwise, convectively unstable. After the substitution of the normal modes, the linearised governing equations become

$$\mathrm{i}k\tilde{v}_x^{(i)} + D\tilde{v}_y^{(i)} = 0, \tag{2.8a}$$

$$Re[-\mathrm{i}\omega\tilde{v}_x^{(i)} + \mathrm{i}k\bar{v}_x^{(i)}\tilde{v}_x^{(i)} + \tilde{v}_y^{(i)}D\bar{v}_x^{(i)}] = -\mathrm{i}k\tilde{p}^{(i)} + \mu^{(i)}(D^2 - k^2 - m^2)\tilde{v}_x^{(i)}, \tag{2.8b}$$

$$Re[-\mathrm{i}\omega\tilde{v}_y^{(i)} + \mathrm{i}k\bar{v}_x^{(i)}\tilde{v}_y^{(i)}] = -D\tilde{p}^{(i)} + \mu^{(i)}(D^2 - k^2 - m^2)\tilde{v}_y^{(i)}, \tag{2.8c}$$

$$Re[-\mathrm{i}\omega\tilde{v}_z^{(i)} + \mathrm{i}k\bar{v}_x^{(i)}\tilde{v}_z^{(i)}] = -\mathrm{i}m\tilde{p}^{(i)} + \mu^{(i)}(D^2 - k^2 - m^2)\tilde{v}_z^{(i)}, \tag{2.8d}$$

$$Re\,Pr[-\mathrm{i}\omega\tilde{T}^{(i)} + \mathrm{i}k\bar{v}_x^{(i)}\tilde{T}^{(i)} + D\bar{T}^{(i)}\tilde{v}_y^{(i)}] = \kappa^{(i)}(D^2 - k^2 - m^2)\tilde{T}^{(i)}, \tag{2.8e}$$

where $D = \mathrm{d}/\mathrm{d}y$.

The above equations are to be solved using the following boundary conditions. At $y = 0$ and $y = 1$, the assumption of no-slip, impermeability and imposed temperature gradient along the plates gives

$$\tilde{v}_x^{(1)} = 0; \quad \tilde{v}_y^{(1)} = 0; \quad \tilde{v}_z^{(1)} = 0; \quad \tilde{T}^{(1)} = 0, \quad \text{at } y = 0, \tag{2.9a}$$

$$\tilde{v}_x^{(2)} = 0; \quad \tilde{v}_y^{(2)} = 0; \quad \tilde{v}_z^{(2)} = 0; \quad \tilde{T}^{(2)} = 0, \quad \text{at } y = 1. \tag{2.9b}$$

At $y = H$, oscillations of the fluid–fluid interface will be induced due to the perturbations. Thus, the infinitesimal displacement of the interface will play a role. These boundary conditions, after substitution of the normal modes, become

$$\mathrm{i}(k\bar{v}_x^{(1)} - \omega)\tilde{\xi} = \tilde{v}_y^{(1)}, \tag{2.9c}$$

$$\tilde{v}_x^{(1)} + D\bar{v}_x^{(1)}\tilde{\xi} = \tilde{v}_x^{(2)} + D\bar{v}_x^{(2)}\tilde{\xi}, \tag{2.9d}$$

$$\tilde{v}_y^{(1)} = \tilde{v}_y^{(2)}, \tag{2.9e}$$

$$\tilde{v}_z^{(1)} = \tilde{v}_z^{(2)}, \tag{2.9f}$$

$$D\tilde{v}_x^{(1)} + \mathrm{i}k\tilde{v}_y^{(1)} + [D^2\bar{v}_x^{(1)} - \mu_r D^2\bar{v}_x^{(2)}]\tilde{\xi} = \mu_r(D\tilde{v}_x^{(2)} + \mathrm{i}k\tilde{v}_y^{(2)}) - \mathrm{i}kMa(\tilde{T}^{(1)} + D\bar{T}^{(1)}\tilde{\xi}), \tag{2.9g}$$

$$D\tilde{v}_z^{(1)} + \mathrm{i}m\tilde{v}_y^{(1)} = \mu_r(D\tilde{v}_z^{(2)} + \mathrm{i}m\tilde{v}_y^{(2)}) - \mathrm{i}mMa(\tilde{T}^{(1)} + D\bar{T}^{(1)}\tilde{\xi}), \tag{2.9h}$$

$$-\tilde{p}^{(1)} + 2Dv_y^{(1)} = -\tilde{p}^{(2)} + 2\mu_r Dv_y^{(2)} - Ca^{-1}(k^2 + m^2)\tilde{\xi}, \tag{2.9i}$$

$$\tilde{T}^{(1)} + D\bar{T}^{(1)}\tilde{\xi} = \tilde{T}^{(2)} + D\bar{T}^{(2)}\tilde{\xi}, \tag{2.9j}$$

$$D\tilde{T}^{(1)} = \kappa_r D\tilde{T}^{(2)}, \tag{2.9k}$$

where all quantities are evaluated at $y = H$.

3. Numerical approach

To carry out the GLSA of the problem at hand, the pseudo-spectral method is employed in which the eigenfunctions corresponding to each dynamic field are expanded into a series

of Chebyshev polynomials as

$$\tilde{f}(y) = \sum_{m=0}^{m=N} a_m \mathcal{T}_m(y), \tag{3.1}$$

where $\mathcal{T}_m(y)$ are Chebyshev polynomials of degree m and N is the highest degree of the polynomial in the series expansion or, equivalently, the number of collocation points. The series coefficients a_m are the unknowns to be solved for. The generalized eigenvalue problem is constructed in the form

$$\boldsymbol{Ae} + \omega \boldsymbol{Be} = 0, \tag{3.2}$$

where $\boldsymbol{A}$ and $\boldsymbol{B}$ are matrices obtained from the discretisation procedure and $\boldsymbol{e}$ is the vector containing the coefficients of all series expansions.

The details of the discretisation of the governing equations and boundary conditions, and construction of $\boldsymbol{A}$ and $\boldsymbol{B}$ can be found in the standard procedure described by Trefethen (2000) and Schmid & Henningson (2001). Application of the pseudo-spectral method for similar problems can be found in the study of Boomkamp *et al.* (1997), Barmak *et al.* (1994), Patne, Agnon & Oron (2020, 2021); Patne *et al.* (2022). The MATLAB routine *eig* is used to solve the constructed generalized eigenvalue problem equation (3.2).

To identify genuine modes in the numerically computed spectrum, the eigenspectrum is obtained for N and $N + 2$ collocation points, which are then compared with a specified tolerance, e.g. 10^{-4}. The genuine eigenvalues are further verified by increasing the number of collocation points by 25 and monitoring the variation of the obtained eigenvalues. If the eigenvalue does not change up to a prescribed precision, e.g. to the sixth significant digit, the same number of collocation points are used to determine the critical parameters of the system. In the present work, $N = 50$ is found to be sufficient to achieve convergence and determine the leading, most unstable eigenvalue within the investigated parameter range.

It must be noted that the numerical and analytical approaches employed here are similar to the one used for studying the stability of a non-isothermal two-layer plane Couette flow by Patne *et al.* (2022). Additionally, for an isothermal two-layer Poiseuille flow, we have validated the asymptotic approach against the standard procedure developed by Yih (1967) and Yiantsios & Higgins (1988) as follows.

To standardise and compare with their predictions, the layers are assumed to be of equal thickness, the relation $\omega = kc$ is used, and the coordinate system origin is shifted to the fluid–fluid interface so that the interface lies at $y = 0$ and fluids 1 and 2 will be present in the intervals $[0, 1]$ and $[0, -1]$, respectively. This adjustment then modifies the base state (2.6) and boundary conditions (2.3) location to mimic Yih (1967) and Yiantsios & Higgins (1988). Now following the procedure for the long-wave asymptotic analysis outlined in § 4, we obtain

$$c_0 = 1 + \frac{2(\mu_r - 1)^2}{\mu_r^2 + 14\mu_r + 1} \tag{3.3}$$

in exact agreement with equation (46) of Yih (1967) and equation (9) of Yiantsios & Higgins (1988) for $n = 1$. Please note that they use m to denote the viscosity ratio μ_r and n to denote the thickness ratio H. Next, we proceed with the $O(k)$ eigenvalue correction for which term-by-term comparison is difficult, thus, the unstable eigenvalue for a particular value of μ_r is compared. For $n = 1$ and $m = 10$, the continuous curve in figure 2(*a*) of Yiantsios & Higgins (1988) gives $c_1/(kRe) \sim 0.0128$ while our procedure followed here predicts $c_1//(kRe) = 0.0127$, which is in excellent agreement thereby validating the long-wave asymptotic analysis. The results obtained by the numerical calculations are

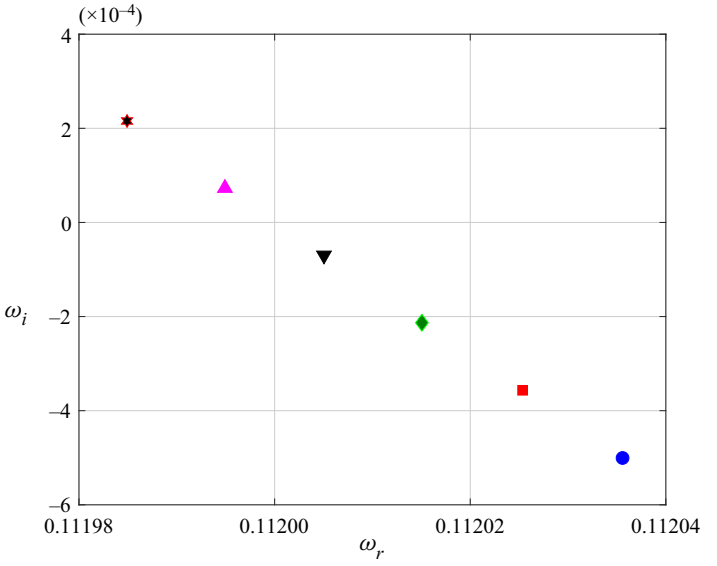

Figure 2. The effect of the variation in Ma on the streamwise mode in the $\omega_r - \omega_i$ plane at $Re = 10$, $H = 0.4$, $\mu_r = 0.5$, $\kappa_r = 1$, $k = 0.1$, $Ca = 0.001$, $m = 0$, and $Pr = 7$. The eigenvalues in the figure correspond to a decreasing Ma in steps of unity such that the blue circle with $\omega_i < 0$ is for $Ma = 0$ and the star with $\omega_i > 0$ is for $Ma = -5$. The figure demonstrates the strong destabilising effect of the thermocapillary stresses on the growth rate of the unstable mode.

then verified against the predictions of the standardised long-wave asymptotic analysis, as shown in figure 4, thus validating the former.

4. General linear stability analysis

Before proceeding with the results, an estimation of the practical range of the dimensionless parameters is presented here. In this case, the typical ranges for the physical properties are (Ezersky *et al.* 1993; De Saedeleer *et al.* 1996; Li, Xu & Kumacheva 2000; Schatz & Neitzel 2001; Ospennikov & Schwabe 2004; Mizev & Schwabe 2009) $R \sim 10^{-6} - 10^{-2}\,\mathrm{m}$, $\rho \sim 10^{3}\,\mathrm{kg\,m^{-3}}$, $\sigma_0 \sim 10^{-3} - 10^{-1}\,\mathrm{N\,m^{-1}}$, $\gamma \sim 10^{-5} - 10^{-3}\,\mathrm{N\,(m\,K)^{-1}}$, $\kappa \sim 10^{-2} - 10^{2}\,\mathrm{J\,(m\,s\,K)^{-1}}$, $\mu \sim 10^{-5} - 10^{2}\,\mathrm{Pa\,s}$ and $V_I \sim 10^{-3} - 10^{-1}\,\mathrm{m\,s^{-1}}$. Thus, the typical dimensionless numbers are $Re \sim O(10^{-5} - 10^{3})$, $Ca \sim O(10^{-4} - 10^{-1})$ and $Pr \sim O(10^{-3} - 10^{3})$. This parametric range will be used here to study the predicted instabilities.

As explained in § 1, the thermocapillary stresses exerted by the fluid layers exhibit strong competition and may influence the stability of the flow. Figure 2 shows the strong destabilising effect of the thermocapillary stresses, which results in instability. The role of the thermocapillary stresses along the interface becomes clear from figure 3. Additionally, figure 3(*b*) shows that as $k \ll 1$, the growth rate $\omega_i \neq 0$, thereby illustrating the long-wave nature of the instability. Figures 2 and 3 show the streamwise mode ($m = 0$). A similar spanwise unstable mode ($k = 0$) also exists with $\omega_r = 0$, thus, a stationary mode. The long-wave streamwise and spanwise modes are amenable to the asymptotic approach with asymptotic expansion around the limit $k = m = 0$. For the convenience of the mathematical analysis and presentation of the results, the discussion will be divided into two sections dealing with the streamwise and spanwise modes.

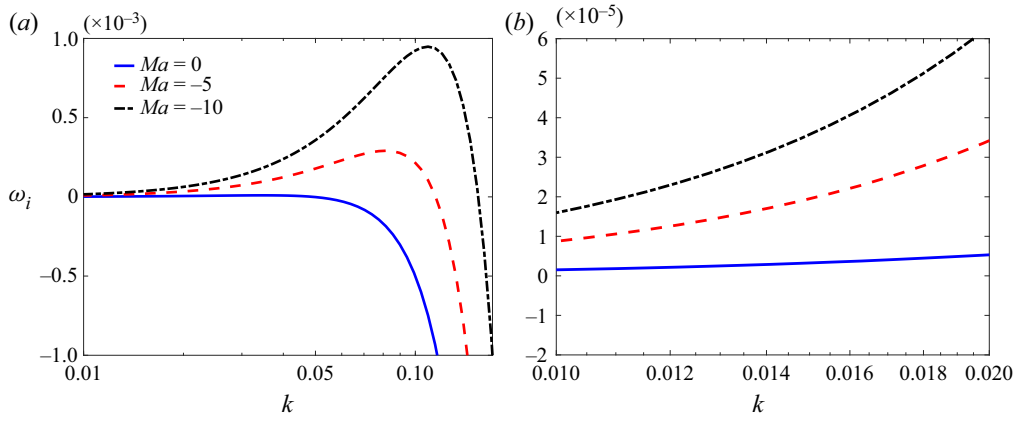

Figure 3. The variation of ω_i with k for the streamwise mode at $Re = 10, H = 0.4, \mu_r = 0.5, \kappa_r = 1, Ca = 0.001, m = 0$ and $Pr = 7$. Panel (a) shows the destabilising effect of decreasing Ma on the streamwise mode. Panel (b) provides the magnified view of the streamwise mode at low k to show that $\omega_i \neq 0$ for $k \ll 1$, thereby illustrating the long-wave nature of the streamwise mode.

4.1. *Streamwise mode ($m = 0$)*

For $m = 0$ and $\tilde{v}_z = 0$, the momentum perturbation equations in (2.8) can be reduced to two-dimensional Orr–Sommerfeld equations

$$\mathrm{i}Re(k\bar{v}_x^{(i)} - \omega)(D^2 - k^2)\tilde{v}_y^{(i)} = \mu^{(i)}(D^2 - k^2)^2\tilde{v}_y^{(i)} - \mathrm{i}kReD^2\bar{v}_x^{(i)}\tilde{v}_y^{(i)}, \tag{4.1}$$

whereas the energy equation in (2.8) is modified by substituting $m = 0$. Next, the velocity and temperature fields and the complex frequency ω are expanded as the series in terms of a small wavenumber k, as

$$\tilde{v}_y^{(i)} = v_{y0}^{(i)} + kv_{y1}^{(i)} + k^2v_{y2}^{(i)} + \cdots, \tag{4.2a}$$

$$\omega = kc_0 + k^2c_1 + k^3c_2 + \cdots, \tag{4.2b}$$

$$\tilde{T}^{(i)} = \frac{1}{k}T_0^{(i)} + T_1^{(i)} + kT_2^{(i)} + \cdots. \tag{4.2c}$$

The above expansions are then substituted into the Orr–Sommerfeld equation (4.1), the energy equation (2.8*e*) and the boundary conditions (2.9). Similar expansion in powers of k for $\tilde{v}_x^{(i)}$ can be obtained from the continuity equations and, for $\tilde{p}^{(i)}$, can be obtained from the x-momentum equation.

At $O(1)$, the governing equations read

$$D^4v_{y0}^{(i)} = 0; \quad D^2T_0^{(i)} = 0. \tag{4.3a,b}$$

Using the expansions (4.2), the $O(1)$ eigenvalue is

$$c_0 = -\frac{[(H^2 - 2H)(\mu_r - 1) - 1][1 + H^2(\mu_r - 1)]}{1 + H(\mu_r - 1)[4 - 6H + 4H^2 - H^3 + H^3\mu_r]}. \tag{4.4}$$

The $O(1)$ eigenvalue, c_0, is a real quantity, thus, these are purely travelling disturbances. For $H = 0.5$, the above expression reduces to equation (46) of Yih (1967), thereby validating the procedure. The above expression is independent of the capillary number

Ca in agreement with Yih (1967). Furthermore, c_0 for both the flows is independent of κ_r, representing the thermal conductivity stratification, and Ma, reflecting the thermal stresses. This implies that the thermocapillarity and thermal properties do not affect the phase speed of the disturbances, while they might affect at $O(k)$ or higher. Thus, we proceed with higher-order correction, i.e. $O(k)$.

At $O(k)$, the governing equations are

$$\mu^{(i)}D^4v_{y1}^{(i)} + \mathrm{i}Re(c_0 - \bar{v}_x^{(i)})D^2v_{y0}^{(i)} - ReD^2\bar{v}_x^{(i)}v_{y0}^{(i)} = 0, \tag{4.5a}$$

$$\kappa^{(i)}D^2T_1^{(i)} + \mathrm{i}Re\,Pr(c_0 - \bar{v}_x^{(i)})T_0^{(i)} - Re\,Pr D\bar{T}^{(i)}v_{y0}^{(i)} = 0. \tag{4.5b}$$

Solving (4.5) in the same way as for $O(1)$ above, yields

$$c_1 = \mathrm{i}\,[f_1(H, \mu_r, \kappa_r)\,Ma + f_2(H, \mu_r)\,Re], \tag{4.6}$$

where

$$f_1 = \frac{g_1}{g_2}; \quad f_2 = \frac{g_3}{g_4}, \tag{4.7a}$$

$$g_1 = (H-1)^2H^2(2H - H^2 + \mu_rH^2 - 1), \tag{4.7b}$$

$$g_2 = [1 + (\kappa_r - 1)H]\,[2 + 2H(\mu_r - 1)(4 - 6H + 4H^2 - H^3 + \mu_rH^3)], \tag{4.7c}$$

$$\begin{aligned} g_3 = &-(2H - H^2 + \mu_rH^2 - 1)\{1 - \mu_r + 5H^{14}(\mu_r - 1)^7(1 + \mu_r) + 2H(-4 + 3\mu_r + \mu_r^2) \\ &-2H^{13}(\mu_r - 1)^6(-32 + 19\mu_r + 3\mu_r^2) + H^{12}(\mu_r - 1)^5(377 - 694\mu_r + 177\mu_r^2) \\ &+H^2(13 + 4\mu_r + 15\mu_r^2 - 32\mu_r^3) + 8H^3(13 - 34\mu_r + 16\mu_r^2 + 5\mu_r^3) \\ &-8H^{11}(\mu_r - 1)^4(-169 + 472\mu_r - 258\mu_r^2 + 29\mu_r^3) \\ &-2H^5(\mu_r - 1)^2(-1144 + 1441\mu_r - 1107\mu_r^2 + 112\mu_r^3) \\ &+2H^9(\mu_r - 1)^3(-2860 + 8635\mu_r - 4718\mu_r^2 + 223\mu_r^3) \\ &+H^8(\mu_r - 1)^3(7293 - 17490\mu_r + 5341\mu_r^2 + 472\mu_r^3) \\ &+H^6(\mu_r - 1)^2(-4719 + 9240\mu_r - 6473\mu_r^2 + 776\mu_r^3) \\ &+H^4(-715 + 1925\mu_r - 2061\mu_r^2 + 1259\mu_r^3 - 408\mu_r^4) \\ &-16H^7(\mu_r - 1)^2(-429 + 1155\mu_r - 873\mu_r^2 + 112\mu_r^3 + 14\mu_r^4) \\ &+H^{10}(\mu_r - 1)^3(3289 - 11517\mu_r + 9743\mu_r^2 - 2115\mu_r^3 + 88\mu_r^4)\}, \end{aligned} \tag{4.7d}$$

$$g_4 = 420(1 + H(4 - 6H + 4H^2 - H^3 + \mu_rH^4)(\mu_r - 1))^3\mu_r^2. \tag{4.7e}$$

Using (4.4) and (4.6), the eigenvalue ω up to $O(k)$ correction is

$$\omega = kc_0(H, \mu_r) + \mathrm{i}\,k^2\,[f_1(H, \mu_r, \kappa_r)\,Ma + f_2(H, \mu_r)\,Re]. \tag{4.8}$$

The function $f_1(H, \mu_r, \kappa_r)$ represents the combined effect of the thermocapillarity and viscosity stratification along the interface while the function $f_2(H, \mu_r)$ represents the inertial stresses alone. The function $f_2(H, \mu_r)$ is similar to the coefficient of Re in the analysis of Yih (1967), thus representing the shear-flow instability due to the viscosity stratification in the absence of an imposed temperature gradient. The first function $f_1(H, \mu_r, \kappa_r)$ is dependent on both the viscosity and thermal conductivity stratification

and represents an additional term due to the imposed temperature gradient. Clearly, the mechanism responsible for the instability stems from shearing action (*Re* term) along the interface, which results in the 'shear-flow mode' and thermocapillary stresses (*Ma* term) along the interface, which leads to the 'thermocapillary mode'. Additionally, from (4.8), the long-wave instability is independent of *Pr*, which is present only in the energy equation as a coefficient of the convection term. Thus, although the momentum convection terms affect the long-wave instability (through the *Re* term), the energy convection does not affect the long-wave instability. The effect of the energy appears only through the Marangoni terms implying the vital role played by the thermocapillary stresses (through the *Ma* term) in determining the stability of the flow.

From (4.8), the instability can exist ($\omega_i > 0$) for an arbitrary Re and $Ma > 0$ if $f_1 > 0$ and $f_2 > 0$. When $f_1 > 0$ and $f_2 < 0$, then a minimum value of $Ma > 0$ will be necessary to set in the instability. If $f_1 < 0$ and $f_2 > 0$ then the flow is unconditionally unstable for $Ma < 0$, implying the necessity of a negative temperature gradient across fluid 1. For $f_1 < 0$ and $f_2 < 0$, a minimum value of $Ma < 0$ is necessary to make flow unstable. Thus, the rest of the analysis aims to evaluate the required critical value and sign of the critical Marangoni number Ma_c to stabilise/destabilise the flow. Equating the imaginary part of (4.8) to zero, we obtain the expression for the critical Marangoni number

$$Ma_c = -\frac{f_2(H, \mu_r)}{f_1(H, \mu_r, \kappa_r)} Re, \tag{4.9}$$

implying Re merely enters as a multiplier; thus, in the present study we have presented and discussed the results for the temporal instability for a fixed $Re = 0.1$.

The comparison of the growth rate (ω_i) of the unstable streamwise mode predicted by the numerical approach and the asymptotic approach (4.6) is presented in figure 4. On expected lines, the asymptotic and numerical approaches are in excellent agreement for $k < 0.5$. From the $O(k)$ expression for the eigenvalue, the shear-flow instability is independent of Ca. To accommodate this in the numerical approach, $Ca = \infty$ has been used.

The orthonormalised velocity and temperature perturbations for the streamwise mode are shown in figure 5. The eigenfunctions vanish at the boundaries of the channel, i.e. $y = 0$ and $y = 1$ due to the impermeability condition and the absence of the temperature perturbations at the wall given by boundary conditions (2.9*a*) and (2.9*b*). Also, both the eigenfunctions achieve maximum at the interface, implying that the instability is driven by the shear and thermocapillary stresses at the interface.

The critical parameter curves (corresponding to $\omega_i = 0$) in $Ma_c - H$ parametric space as a function of μ_r and κ_r are shown in figure 6. From (4.7*a*), (4.7*b*) and (4.7*d*), the factor $(2H - H^2 + \mu_r H^2 - 1)$ is common in the numerator for both $f_1(H, \mu_r, \kappa_r)$ and $f_2(H, \mu_r)$ with g_3 having a negative sign preceding the factor, thus, both functions have a common root $H = (\sqrt{\mu_r} - 1)/(\mu_r - 1)$. The remaining factors of g_1, namely, $(H - 1)^2$, H^2 and g_2 do not affect the sign of f_1 for $\mu_r < 1$. Similarly, the remaining factors of g_3 and g_4 do not affect the sign of f_2. Thus, for a given value of H and μ_r, both functions will possess an opposite sign and their signs will switch at the root $H = (\sqrt{\mu_r} - 1)/(\mu_r - 1)$. This is precisely the case depicted in figure 6 with the location of the vertical line parallel to the Ma_c axis indicating the root. For example, for $\mu_r = 0.1$, the root is $H = 0.76$ with $f_1 > 0$ and $f_2 < 0$ for $H < 0.76$ and $f_1 < 0$ and $f_2 > 0$ for $H > 0.76$ separated by a vertical line at $H = 0.76$ in figure 6(*a*). Thus, for $Ma > 0$, for $H < 0.76$, the thermocapillarity stabilises while the shear force has a destabilising influence. The opposite is the case for $f_1 < 0$ and

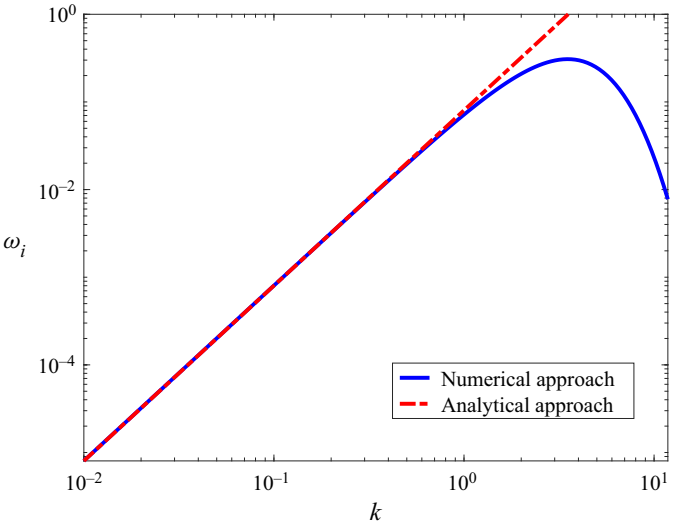

Figure 4. Comparison between the asymptotic and numerical approaches in the prediction of the growth rate ω_i with wavenumber k at $Re = 0.1$, $H = 0.3$, $\mu_r = 0.3$, $\kappa_r = 3$, $Ca = \infty$ and $Pr = 7$ for the return flow. The excellent agreement between the asymptotic and numerical approaches for $k < 0.5$ validates the numerical methodology utilised here. For $\omega_i > 0$, the flow is unstable.

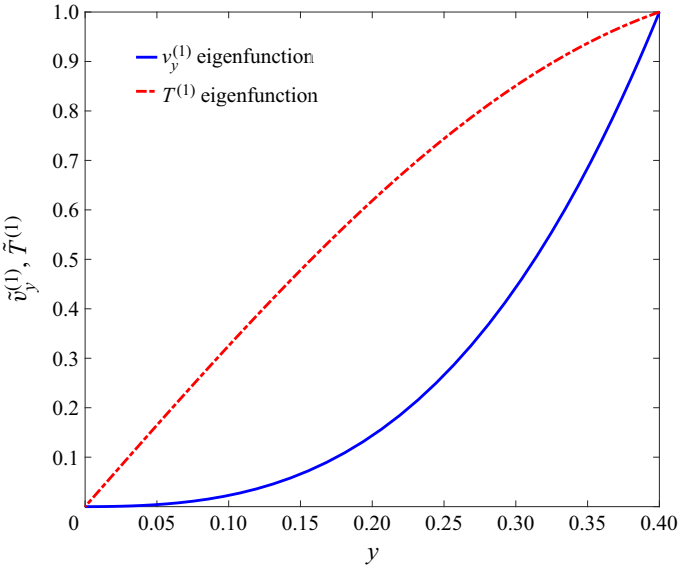

Figure 5. The variation of the orthonormalised velocity and temperature eigenfunctions (for fluid 1) in the x–y plane at $Re = 10$, $Pr = 7$, $\mu_r = 0.5$, $H = 0.4$, $\kappa_r = 1$, $Ma = -10$, $Ca = 0.001$ and $k = 0.1$ for the streamwise mode $\omega = 0.111936 + 0.000924\,\mathrm{i}$. The eigenfunctions exhibit maximum variation near $y = 0.4$, i.e. the interface, indicating the destabilisation introduced by the shearing and thermocapillary stresses along the interface. The plotted eigenfunctions are the modulus or absolute value of the respective eigenfunctions.

$f_2 > 0$ for $H > 0.76$. Also, the root $H = (\sqrt{\mu_r} - 1)/(\mu_r - 1)$ is independent of κ_r, thus, variation in κ_r does not affect the location of the vertical line shown in figure 6.

For $\mu_r > 1$, as shown in figure 6(*b*), a negative temperature gradient is necessary to stabilise or destabilise the flow. In this case, functions f_1 and f_2 have $H = 0.24$ as the

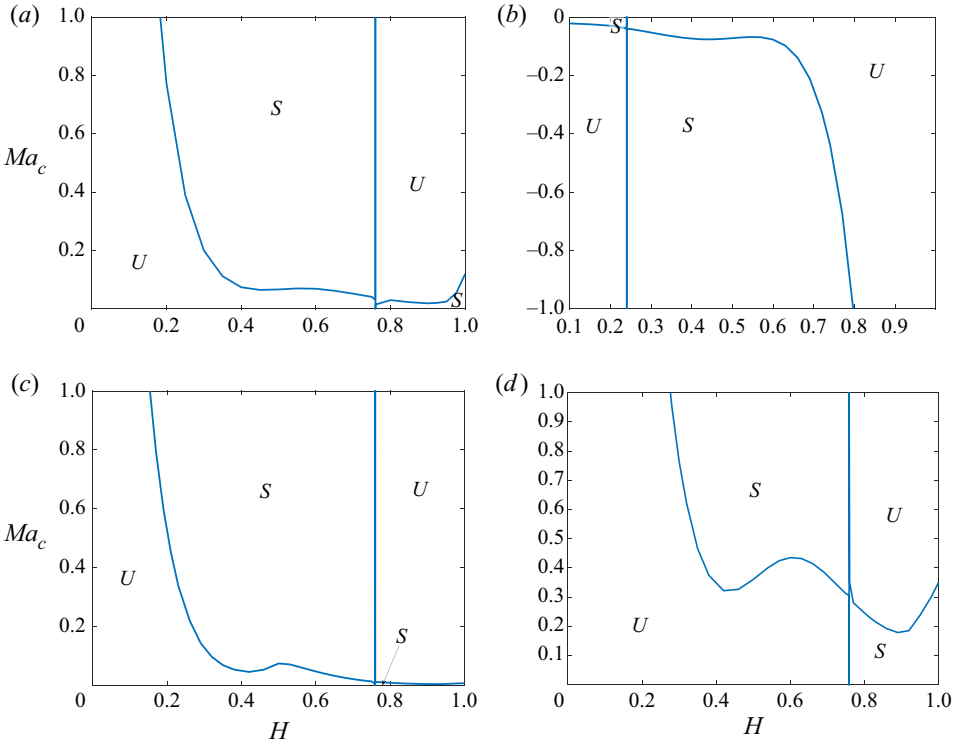

Figure 6. Variation in the critical Marangoni number Ma_c with the relative position of the interface H at $Re = 0.1$. The capillary number Ca and Prandtl number Pr do not affect the critical parameters for the long-wave instability, as seen in (4.8). (*a*) For $H < 0.76$, $f_1 < 0$ and $f_2 > 0$; thus, the thermocapillarity has a stabilising effect (if $\beta_1 > 0$) while the shearing force has a destabilising effect. As a result, the flow is unstable for $Ma < Ma_c$. However, for $H > 0.76$, $f_1 > 0$ and $f_2 < 0$, which leads to the swapping of the stable and unstable regimes. (*b*) For $H < 0.24$, $f_1 < 0$ and $f_2 < 0$; thus, both thermocapillarity and the shearing force have a stabilising effect (if $\beta_1 > 0$). However, if $\beta_1 < 0$ then the flow becomes unstable for $Ma < 0$. For $H > 0.24$, the shearing force has a destabilising effect, while thermocapillarity with β_1 has a stabilising effect. (*c*) A decreasing κ_2 or an increasing κ_1 shifts the neutral stability boundary to a lower Ma. (*d*) Illustrates the opposite scenario of panel (*c*). Results are shown for (*a*) $\kappa_r = 1$ and $\mu_r = 0.1$, (*b*) $\kappa_r = 1$ and $\mu_r = 10$, (*c*) $\kappa_r = 0.1$ and $\mu_r = 0.1$, (*d*) $\kappa_r = 10$ and $\mu_r = 0.1$.

common root. For $H < 0.24$, both f_1 and f_2 are negative, thus, both the thermocapillary and inertial terms have a stabilising influence due to which a negative temperature gradient is necessary to set in the instability. While for $H > 0.24$, both f_1 and f_2 are positive, thus, both the thermocapillary and inertial terms have a destabilising influence. A negative temperature gradient then becomes necessary to stabilise the flow. The physical mechanism of the stabilisation or destabilisation due to the viscosity stratification, i.e. impact of variation in the parameter μ_r is explained in § 5.

The effect of the thermal conductivity stratification on the stable and unstable zones in $Ma_c - H$ parametric space is shown in figure 6(*c*,*d*). Figure 6(*c*) shows that if fluid 2 has a lower thermal conductivity than fluid 1, i.e. $\kappa_r < 1$, then compared with the only viscosity stratification shown in figure 6(*a*), the critical parameter curves shift to a lower Ma_c while the opposite occurs for $\kappa_r > 1$. The physical picture of the impact of variation in the parameter κ_r on the thermocapillary mode is discussed in § 5.

The analysis of Wei (2006), which considered a two-layer plane Couette flow subjected to a temperature gradient, assumed one of the fluid layers in the thin-film limit implied

$H \to 0$ or $H \to 1$. He concluded that the shear-flow mode could be stabilised for an arbitrary H by the thermocapillary mode. However, from figure 6, for $\mu_r < 1$, the thermocapillarity is unable to stabilise the flow as $H \to 0$ while, for $\mu_r > 1$, again thermocapillarity is incapable of stabilising the flow as $H \to 1$. This implies that the analysis of Wei (2006) has limited applicability to a two-layer pressure-driven flow subjected to a temperature gradient. Furthermore, Wei (2006) predicted two neutral states when the interface tension is weak, but there is no such region found in the present analysis highlighting the difference between the two-layer planar Couette and pressure-driven flows or a possible failure of the thin-film assumption of Wei (2006).

4.2. *Spanwise mode ($k = 0$)*

For $k = 0$ and $\tilde{v}_x = 0$, the momentum perturbation equations in (2.8) reduce to

$$-\mathrm{i}\omega\, Re(D^2 - m^2)\tilde{v}_y^{(i)} = \mu^{(i)}(D^2 - m^2)^2\tilde{v}_y^{(i)}, \tag{4.10}$$

and the energy equations in (2.8) are modified by substituting $k = 0$ and $\tilde{v}_x = 0$. Similar to the case of the streamwise perturbations, the velocity and temperature fields and the complex frequency ω are expanded as the series in terms of spanwise wavenumber m,

$$\tilde{v}_y^{(i)} = v_{y0}^{(i)} + m v_{y1}^{(i)} + m^2 v_{y2}^{(i)} + \cdots, \tag{4.11}$$

$$\omega = mc_0 + m^2 c_1 + m^3 c_2 + \cdots, \tag{4.12}$$

$$\tilde{T}^{(i)} = \frac{1}{m}T_0^{(i)} + T_1^{(i)} + mT_2^{(i)} + \cdots. \tag{4.13}$$

The above expansions are then substituted in (4.10), the energy equation (2.8*e*) for $k = 0$ and the boundary conditions (2.9). The expansions in powers of m for $\tilde{v}_x^{(i)}$ and $\tilde{p}^{(i)}$ are obtained from the continuity equations and the z-momentum equations, respectively.

At $O(1)$, the governing equations read

$$D^4 v_{y0}^{(i)} = 0; \quad D^2 T_0^{(i)} = 0. \tag{4.14a,b}$$

At $O(1)$, the eigenvalue is

$$c_0 = 0. \tag{4.15}$$

This shows that the spanwise mode is stationary. At $O(m)$, the governing equations are

$$\mu^{(i)} D^4 v_{y1}^{(i)} + \mathrm{i}Re c_0 D^2 v_{y0}^{(i)} = 0, \tag{4.16a}$$

$$D^2 T_1^{(i)} + \mathrm{i}Re\, Pr c_0 T_0^{(i)} - Re\, Pr \frac{\partial \bar{T}^{(i)}}{\partial y} v_{y0}^{(i)} = 0. \tag{4.16b}$$

Solving (4.16) in the same way as for $O(1)$ above, yields

$$c_1 = \mathrm{i} f_1(H, \mu_r, \kappa_r)\, Ma, \tag{4.17}$$

where f_1 is a function defined in (4.7*a*). Using (4.15) and (4.17), the eigenvalue ω up to $O(m)$ correction is

$$\omega = \mathrm{i}\, m^2 f_1(H, \mu_r, \kappa_r)\, Ma. \tag{4.18}$$

A comparison of the above expression for ω with the expression for the complex frequency for the streamwise mode (4.8) shows the absence of the shear-flow term (i.e. Re term)

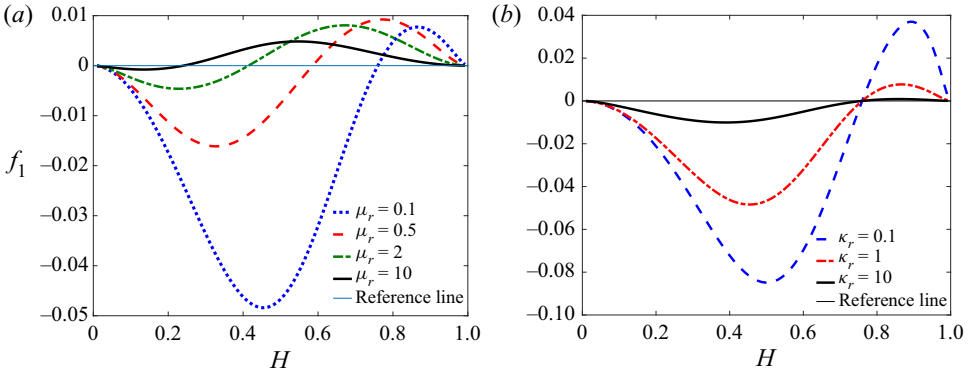

Figure 7. Variation of the function f_1 with the relative position of the liquid–liquid interface H. (a) An increasing μ_r increases the range of H for which $f_1 > 0$. (b) A decreasing κ_r increases maximum $|f_1|$ values. The spanwise mode is unstable for the H range that satisfies the condition $f_1 > 0$. Results are shown for (a) $\kappa_r = 1$, (b) $\mu_r = 0.1$.

for the spanwise mode. The shear-flow term is absent since the base-state flow is only in the streamwise direction, while there is no base-state velocity present in the spanwise direction. This is also the reason that the $O(1)$ eigenvalue vanishes, thereby implying a stationary mode.

From (4.18), the spanwise mode is unstable if the product $f_1 Ma > 0$. From figure 7(a), for a given μ_r, there exists a range of H for which $f_1 > 0$. For such a range, the spanwise perturbations become unstable for a positive temperature gradient, i.e. $Ma > 0$. While for $f_1 < 0$, a negative temperature gradient, i.e. $Ma < 0$, is essential for destabilising the spanwise mode. For example, from the curve for $\mu_r = 0.1, f_1 < 0$ for $H < 0.76$ and $f_1 > 0$ for $H > 0.76$; thus, to destabilise the spanwise perturbations, $Ma < 0$ for $H < 0.76$ and $Ma > 0$ for $H > 0.76$ will be necessary.

The dominant mode of instability, i.e. the mode with the higher growth rate between the streamwise and spanwise modes, and its range can be decided as follows. When $f_2 < 0$, then from (4.8), the streamwise mode will have to overcome the stabilising effect of the inertial term to destabilise the flow, which is not the case with the spanwise mode since the inertial term is absent (see (4.18)). Thus, the spanwise mode will dominate the stability of the flow in the parametric regime for which $f_2 < 0$. The opposite is true when the inertial term has a destabilising effect, i.e. $f_2 > 0$. In this case, the streamwise mode will have a higher growth rate than the spanwise mode, thereby becoming the dominant mode.

4.3. *Oblique modes*

The above discussion was limited to only the extremes, i.e. streamwise and spanwise instability modes. However, the streamwise and spanwise instability modes turn out to be the dominant modes of instability as follows. A comparison of (4.8) and (4.18) shows that the difference between the two modes is due to the term $f_2(H, \mu_r)Re$. Thus, if $f_2 < 0$ then the spanwise mode will possess a higher growth rate than the streamwise mode, and the opposite will be true for $f_2 > 0$. Any oblique mode with $k \neq 0$ and $m \neq 0$ will have both Ma and Re terms. The function f_1 will remain the same for all oblique modes since it remains the same for the extremes, i.e. streamwise and spanwise modes. However, the Re term will diminish as one goes from a streamwise to spanwise mode. Thus, if $f_2 < 0$, all oblique and streamwise modes will have a growth rate lower than the spanwise

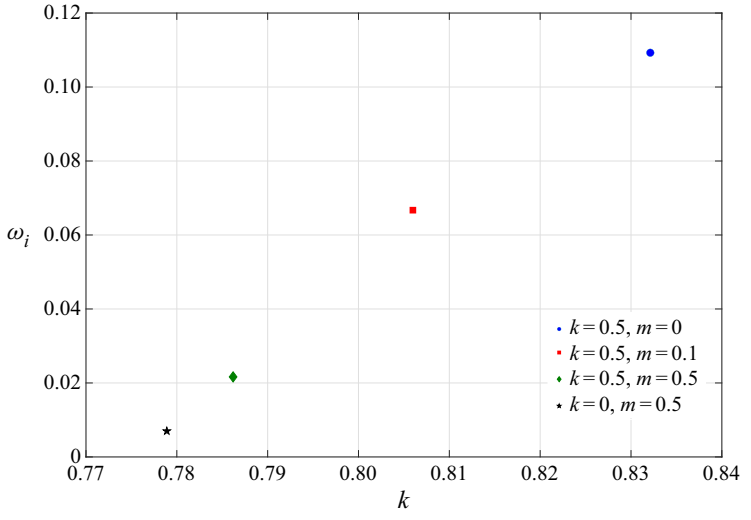

Figure 8. The growth rate variation due to variations in k and m in the $\omega_r - \omega_i$ plane at $Re = 10, H = 0.3, \mu_r = 0.1, \kappa_r = 3, Ma = -10, Ca = 0.01$ and $Pr = 7$. The figure demonstrates that any oblique mode will have a growth rate between the streamwise and spanwise modes. In the illustrated case, $f_2 > 0$, thus, the streamwise mode exhibits a higher growth rate than the oblique and spanwise modes.

mode, while for $f_2 > 0$, the streamwise mode will possess a higher growth rate than oblique and spanwise modes. Thus, the analysis presented here successfully captures the dominant modes of instability, *viz.*, streamwise and spanwise modes. The case with $f_2 > 0$ is illustrated in figure 8.

5. Physical mechanism

5.1. *Purely thermocapillary mode (Re = 0)*

In the following section we discuss the role of shear and Marangoni stresses exerted on the liquid–liquid interface in causing the predicted instabilities. The physical mechanism behind the Marangoni instability in a liquid layer with a free surface subjected to a negative vertical temperature gradient is well understood (Smith & Davis 1983*a*,*b*; Patne *et al.* 2021).

Consider a 'hot spot' generated randomly due to the temperature fluctuations at the interface as schematically shown in figure 9. The surface tension at the hot spot decreases correspondingly, which sets fluid flows away from the hot spot along the interface as shown by arrows pointing away from the hot spot in figure 9. To maintain the local mass conservation, upward and downward flows develop in fluids 1 and 2, respectively. Simultaneously, the hot spot loses thermal energy due to thermal diffusion to the surrounding fluid. These upward and downward flows are also opposed by viscous forces. Thus, the fate of the hot spot, i.e. growth or decay, is determined by the combined effects of the generated flows and the viscosity and thermal diffusivity of the fluids.

For the positive temperature gradient across fluid 1, i.e. $\beta_1 > 0$, the fluid layer adjacent to the interface on the fluid 1 side is at a lower temperature than the interface. The opposite is the case with fluid 2. Thus, the upflow will try to cool down the hot spot while the downflow will try to heat it up. The cooling action of the upflow and the heating action of the downflow will be reinforced/opposed by the viscous forces and thermal diffusion of energy. For example, the cooling action of the upflow reinforces the thermal energy

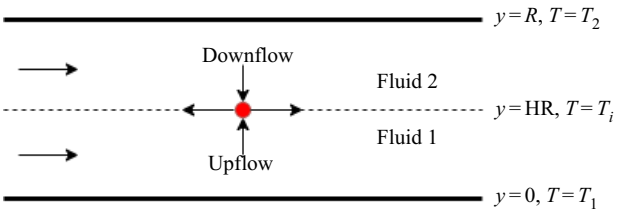

Figure 9. A schematic of the hot spot (red opaque circle) evolution at the interface. The temperature at the interface $T = T_i$ differs from the wall temperatures due to the imposed temperature gradient. The thermocapillarity generates flow away from the hot spot along the interface. To fill in the so-formed mass deficiency, an upflow in fluid 1 and a downflow in fluid 2 emerge. The combination of these flows leads to the stabilising or destabilising effects of the thermocapillary stresses discussed in § 4.

loss due to the thermal diffusion from the hot spot. Thus, for the instability to exist, the downflow must overcome the cooling action of the upflow, viscous forces and the thermal diffusion of the thermal energy that is a function of the parameters H, μ_r and κ_r.

5.1.1. *Effect of H*

Consider the purely thermocapillary mode, which can be effectively represented by figure 7 since only the thermocapillary mode of instability exists for the spanwise mode. For a positive temperature gradient $\beta_1 > 0$, from figure 7, the flow becomes unstable for certain H depending on the value of κ_r implying that as H increases the flow gets destabilised, which can be explained as follows.

As discussed above, for $\beta_1 > 0$, the downflow is responsible for amplifying the hot spot energy, while the upflow, viscous forces and thermal diffusion are responsible for the decrease in the hot spot energy. As H increases, the interface gets closer to the upper plate with a higher temperature implying an increased temperature on the fluid 2 side of the interface. Thus, as the interface moves closer to the upper plate, the heating effect provided by the downflow to the hot spot also increases, which can then overcome the cooling effect provided by the upflow, thereby leading to thermocapillary instability. To generalize, as the interface approaches the hotter fluid side, the thermocapillary instability becomes severe.

5.1.2. *Effect of κ_r*

The hot spot shown in figure 9 can lose thermal energy through diffusion on the fluid 1 side, and the opposite is true on the fluid 2 side since the heat flux due to thermal diffusion is proportional to the negative temperature gradient. At the same time, the downflow loses while upflow gains energy while travelling to the interface by thermal diffusion since the downflow is at a higher temperature than the surrounding while the upflow is at a lower temperature than the surrounding. From figure 7(*b*), as κ_r decreases, the magnitude of f_1 (thus, ω_i) increases, which indicates that a decreasing κ_r has a destabilising effect on the flow. The inequality $\kappa_r < 1$ implies $\kappa_2 < \kappa_1$. The destabilisation thus could be a result of the diffusion-mediated energy gain by the upflow due to higher thermal conductivity and lesser diffusion-mediated energy loss by the downflow, both of which support the increase of hot spot energy. The destabilising effect of decreasing κ_r also implies a minor role played by the energy loss from the hot spot on fluid 1 side by thermal diffusion. For $\beta_1 < 0$, there will be an opposite effect.

5.1.3. *Effect of* μ_r

From figure 7(*a*), as μ_r increases, the flow becomes unstable for a larger range of H, which can be explained as follows. As $\mu_r \gg 1$, the two-layer system approaches the familiar single-layer system subjected to a temperature gradient with fluid 2 having an extremely higher viscosity than fluid 1, much akin to a water layer on a heated substrate and exposed to ambient air. Essentially, one can neglect the dynamics of fluid 1, which is indeed the case in the literature wherever thermocapillary instabilities are studied in a liquid layer (Oron *et al.* 1997). Thus, the increasing unstable H range with increasing μ_r is due to the lower/higher viscous stresses exerted by fluid 1/fluid 2 at the interface. For $\beta_1 < 0$ and $\mu_r \ll 1$, the dynamics of fluid 2 can be neglected based on similar arguments.

5.2. *Purely shear-flow mode (*$Ma = 0$*)*

The mechanism for the shear-flow instability arising due to viscosity stratification was explained by Yih (1967), Hinch (1984), Smith (1990) and Charru & Hinch (2000). For the long-wave instability, the explanation suggested by Charru & Hinch (2000) was that, due to the viscosity stratification, perturbations in the longitudinal velocity component develop, which then lead to the emergence of pressure perturbations. It must be noted that, from (4.8), the shear-flow component of the long-wave instability, i.e. the term containing the Reynolds number Re, remains unaffected by the presence of the Marangoni stresses. Thus, the destabilisation mechanism proposed by Charru & Hinch (2000) for the long-wave instability is also applicable here.

5.3. *Combined thermocapillary and shear-flow mode*

The thermal and velocity perturbations are related by the tangential stress balance conditions (2.9*g*) and (2.9*h*) at the interface and through the base-state–perturbed-state terms in the linearised energy equation (2.8*e*). Thus, when a thermocapillary mode of instability becomes unstable by the mechanism discussed in § 5.1, then the thermal perturbations start to grow, which then leads to the growth of the velocity perturbations through the relations (2.9*g*), (2.9*h*) and (2.8*e*). Similarly, when the shear-flow mode becomes unstable by the mechanism discussed in § 5.2, longitudinal velocity perturbations start to develop. This growth in the velocity perturbations then leads to the growth of the thermal perturbations through the relations (2.9*g*), (2.9*h*) and (2.8*e*). Depending on the stable/unstable nature of both modes, the superposition between the thermocapillary and shear-flow modes can be classified into the following two types.

5.3.1. *Constructive superposition*

Consider the parametric regime where f_1, Ma and f_2 are positive. In this case, both velocity and temperature perturbations start developing, which leads to the reinforcement of the growth of the perturbations due to both shear flow and thermocapillarity through the relations (2.9*g*), (2.9*h*) and (2.8*e*). Thus, shear flow and thermocapillarity help each other in causing the flow to become unstable with the mode possessing a growth rate higher than the individual modes, thereby leading to constructive superposition.

5.3.2. *Destructive superposition*

First, consider the parametric regime with $f_1 > 0, Ma > 0$ and $f_2 < 0$ where the thermocapillarity has a destabilising influence while the shear flow has a stabilising influence. In this case, the developing temperature perturbations due to the

thermocapillarity are suppressed by the stabilising velocity perturbations caused by the imposed shear flow through the relations (2.9*g*), (2.9*h*) and (2.8*e*), thereby leading to the destructive superposition. Thus, for an unstable flow to exist, the shear flow has to overcome the stabilising influence of thermocapillarity. The opposite scenario exists for $f_1 < 0, Ma > 0$ and $f_2 > 0$ or $f_1 > 0, Ma < 0$ and $f_2 > 0$ where the thermocapillarity has a stabilising influence while the shear flow has a destabilising influence that can be explained in a similar manner.

6. Long-wave analysis

To explore the long-wave instability, we derive the long-wave evolution equation describing the dynamics of the liquid layers for the streamwise disturbances. We then carry out the linear and weakly nonlinear analyses of the system. Let λ be the wavelength of the long-wave disturbances such that $R = \epsilon\lambda$, where $\epsilon \ll 1$. Now, following the procedure described in Oron *et al.* (1997), Patne *et al.* (2021) and Samanta (2013) we scale the x axis and time as $x \to X\epsilon^{-1}$ and $t \to \tau\epsilon^{-1}$. While the fluid dynamical quantities are expanded as

$$v_x^{(i)} = u_0^{(i)} + \epsilon u_1^{(i)} + \cdots, \tag{6.1}$$

$$v_y^{(i)} = \epsilon v_0^{(i)} + \epsilon^2 v_1^{(i)} + \cdots, \tag{6.2}$$

$$p^{(i)} = \frac{1}{\epsilon}\Pi_0^{(i)} + \Pi_1^{(i)} + \cdots. \tag{6.3}$$

Using these scalings, at the leading order $O(\epsilon^0)$ the governing equations (2.2) reduce to

$$-\partial_X \Pi_0^{(i)} + \mu^{(i)}\partial_y^2 u_0^{(i)} = 0, \quad \partial_y \Pi_0^{(i)} = 0, \quad \partial_y^2 T^{(i)} = 0. \tag{6.4a–c}$$

Equations (6.4*a–c*) are subjected to the following boundary conditions. At the lower ($y = 0$) and upper ($y = 1$) walls, the assumptions of no-slip, impermeability and fixed temperature imply that

$$\text{at } y = 0, \quad u_0^{(1)} = 0; \quad v_0^{(1)} = 0; \quad T^{(1)} = T_1, \tag{6.5a}$$

$$\text{at } y = 1, \quad u_0^{(2)} = 0; \quad v_0^{(2)} = 0; \quad T^{(2)} = T_2. \tag{6.5b}$$

At the fluid–fluid interface $y = h(x, t)$, the continuity of the tangential velocity, tangential and normal stresses, temperature field and heat flux gives

$$u_0^{(1)} = u_0^{(2)}, \tag{6.5c}$$

$$v_0^{(1)} = v_0^{(2)}, \tag{6.5d}$$

$$\partial_y u_0^{(1)} - \mu_r \partial_y u_0^{(2)} = -\widehat{Ma}(\partial_X T + \partial_y T \partial_X h), \tag{6.5e}$$

$$\Pi_0^{(1)} - \Pi_0^{(2)} = -\widehat{Ca}^{-1}\partial_X^2 h, \tag{6.5f}$$

$$T^{(1)} = T^{(2)}, \tag{6.5g}$$

$$\partial_y T^{(1)} = \kappa_r \partial_y T^{(2)}, \tag{6.5h}$$

where

$$\widehat{Ma} = \epsilon Ma, \quad \widehat{Ca} = \epsilon^{-3} Ca, \tag{6.5i}$$

are the scaled Marangoni and capillary numbers, respectively. Solving $O(\epsilon^0)$ equations (6.4*a–c*) using the boundary conditions (6.5) yield the velocity profiles for the fluids.

In addition to the above boundary conditions, an additional boundary condition related to the volumetric flow rate is imposed to evaluate the pressure gradient (6.6*h*), which at $O(\epsilon^0)$ gives

$$\int_0^h u_0^{(1)} + \int_h^1 u_0^{(2)} = q, \tag{6.5j}$$

where q is the total volumetric flow rate.

The solution of the above system of governing equations (6.4*a–c*) subjected to the boundary conditions (6.5) gives

$$u_0^{(1)} = a_1 + a_2 y + \frac{1}{2}\partial_X \Pi_0^{(1)}, \tag{6.6a}$$

$$u_0^{(2)} = a_3 + a_4 y + \frac{1}{2\mu_r}\partial_X \Pi_0^{(2)}, \tag{6.6b}$$

$$T^{(1)} = t_1 + t_2 y, \tag{6.6c}$$

$$T^{(2)} = t_3 + t_4 y, \tag{6.6d}$$

where a_i and t_i are the integration constants

$$a_1 = 0, \tag{6.6e}$$

$$a_2 = \frac{[1 + H(\kappa_r - 1)]Ma(h-1)\partial_X h}{[1 + (\kappa_r - 1)h]^2[1 + (\mu_r - 1)h]} - \frac{h[2 + (\mu_r - 2)h]\partial_X \Pi_0^{(1)} + (h-1)^2 \partial_X \Pi_0^{(2)}}{2[1 + (\mu_r - 1)h]}, \tag{6.6f}$$

$$a_3 = -\frac{Ma\,(1 - H + H\kappa_r)h\,\partial_X h}{[1 + (\kappa_r - 1)h]^2[1 + (\mu_r - 1)h]} - \frac{\mu_r h \partial_X \Pi_0^{(1)} + [\mu_r + h - 1 - 2\mu_r h]\partial_X \Pi_0^{(2)}}{2[1 + (\mu_r - 1)h]}, \tag{6.6g}$$

$$a_4 = \frac{-\partial_X \Pi_0^{(2)} + h[2Ma\mu_r(1 - H + H\kappa_r)\partial_X h + \mu_r h[1 + (\kappa_r - 1)h]^2 \partial_X \Pi_0^{(1)}]}{2\mu_r[1 + (\kappa_r - 1)h]^2[1 + (\mu_r - 1)h]} + \frac{h[2 - 2\kappa_r + h(-\kappa_r^2 + 2\kappa_r - 2\mu_r - (\kappa_r - 1)(2\mu_r - 1)h(2 + \kappa_r h - h))]\partial_X \Pi_0^{(2)}}{2\mu_r[1 + (\kappa_r - 1)h]^2[1 + (\mu_r - 1)h]}, \tag{6.6h}$$

$$t_2 = \frac{[1 + H(\kappa_r - 1)]\partial_X h}{[1 + (\kappa_r - 1)h]^2}, \tag{6.6i}$$

$$t_4 = \frac{[1 + H(\kappa_r - 1)]\partial_X h}{\kappa_r[1 + (\kappa_r - 1)h]^2}. \tag{6.6j}$$

The exact expressions of t_1 and t_3 are irrelevant in the present analysis and thus not presented here for the sake of brevity. Using the velocity profiles (6.6*a*) and (6.6*b*), the

pressure gradient in the first fluid is

$$\partial_X \Pi_0^{(1)} = -\frac{6\mu_r[2q(1+\kappa_r h-h)^2(1+\mu_r h-h)-Mah(1+H\kappa_r-H)(h-1)\partial_X h]}{[1+(\kappa_r-1)h]^2[1+h(\mu_r-1)(4-6h+4h^2+(\mu_r-1)h^3)]} + \frac{(h-1)^2[-1+2h-4\mu_r h+(\mu_r-1)h^2]\partial_X^3 h}{Ca[1+h(\mu_r-1)(4-6h+4h^2+(\mu_r-1)h^3)]}. \tag{6.6k}$$

The rescaled kinematic boundary condition at the interface up to $O(1)$ is

$$\partial_t h = -\partial_x \int_0^h u_0^{(1)}\,\mathrm{d}y. \tag{6.7}$$

By substituting the velocity profiles derived above into (6.7), the following thickness evolution equation can be obtained:

$$\mathcal{H}_1(h, \partial_x h, \partial_x^2 h, \partial_x^3 h, \partial_x^4 h) + \mathcal{H}_2(h)\partial_t h = 0. \tag{6.8a}$$

At $O(\epsilon)$, the governing equations give

$$Re(\partial_\tau u_0^{(i)} + u_0^{(i)}\partial_X u_0^{(i)} + v_0^{(i)}\partial_y u_0^{(i)}) = -\partial_X \Pi_1^{(i)} + \mu^{(i)}\partial_y^2 u_1^{(i)}, \tag{6.9a}$$

$$\partial_y \Pi_1^{(i)} = 0, \tag{6.9b}$$

where the energy equation is irrelevant and, thus, neglected. The transverse components of velocity $v_0^{(i)}$ can be obtained from the continuity equation

$$v_0^{(1)} = -\int_0^y \partial_x u_0^{(1)}\,\mathrm{d}y, \tag{6.10}$$

$$v_0^{(2)} = -\int_y^1 \partial_x u_0^{(2)}\,\mathrm{d}y. \tag{6.11}$$

At $O(\epsilon)$, the boundary conditions at the wall are,

$$\text{at } y=0, \quad u_1^{(1)} = 0; \quad v_1^{(1)} = 0, \tag{6.12a}$$

$$\text{at } y=1, \quad u_1^{(2)} = 0; \quad v_1^{(2)} = 0. \tag{6.12b}$$

While at the fluid–fluid interface, the interface conditions are

$$u_1^{(1)} = u_1^{(2)}, \tag{6.12c}$$

$$v_1^{(1)} = v_1^{(2)}, \tag{6.12d}$$

$$\partial_y u_1^{(1)} - \mu_r \partial_y u_1^{(2)} = 0, \tag{6.12e}$$

$$\Pi_1^{(1)} - \Pi_1^{(2)} = 0. \tag{6.12f}$$

Similar to the volumetric flow condition (6.5*j*), the volumetric flow condition at $O(\epsilon)$ is

$$\int_0^h u_1^{(1)} + \int_h^1 u_1^{(2)} = 0. \tag{6.12g}$$

Solving the system of (6.9) with boundary conditions (6.12) gives the $O(\epsilon)$ contribution. Unlike $O(\epsilon^0)$ equations, $O(\epsilon)$ equations turn out to be cumbersome to handle even with

the help of MATHEMATICA, thus, explicit expressions for the quantities are not given here. The rescaled kinematic boundary condition at the interface up to $O(\epsilon)$ is

$$\partial_t h = -\partial_x \int_0^h (u_0^{(1)} + u_1^{(1)})\,\mathrm{d}y. \tag{6.13}$$

A similar procedure can also be followed for the spanwise mode ($k = 0$) with the streamwise velocity, scaled axis x, and tangential stress component τ_{yx} being replaced by the spanwise velocity, scaled axis z, and tangential stress component τ_{yz}, respectively. An additional change is the modification of the boundary condition (6.5*j*) by substituting $q = 0$ since there is no volumetric flow rate in the spanwise direction. Thus, the above kinematic boundary condition can be set in the vector form to include the spanwise component.

6.1. *Temporal stability analysis ($k_i = 0$)*

To obtain the dispersion relation, we linearise (6.13) and substitute $h(x, t) = H + \delta \mathrm{e}^{\mathrm{i}(kx-\omega t)}$ where $\delta \ll 1$ in the resulting linearised equation to obtain the dispersion relation

$$\omega = kf_0(H, \mu_r)q + \mathrm{i}\,k^2[f_1(H, \mu_r, \kappa_r)Ma + f_2(H, \mu_r)Re] + \mathrm{i}\,k^4\frac{f_3(H, \mu_r)}{Ca}, \tag{6.14}$$

where f_1 and f_2 are defined in (4.7*a*) and

$$f_0 = \frac{6\mu_r(H-1)H[(H^2-2H)(\mu_r-1)-1][1+H^2(\mu_r-1)]}{[1+H(\mu_r-1)(4-6H+4H^2-H^3+H^3\mu_r)]^2}, \tag{6.15}$$

$$f_3 = \frac{(H-1)^3H^3[1+H(\mu_r-1)]}{3+3H(\mu_r-1)(4-6H+4H^2-H^3+H^3\mu_r)}, \tag{6.16}$$

where the function $f_3 < 0$ for arbitrary μ_r and H. For (4.8) and (6.14) to give the same eigenvalue requires $q = c_0/f_0$, thereby obtaining q. The dispersion relation for the spanwise mode can be simply obtained from (6.14) by substituting $q = 0$, $k = m$ and $Re = 0$,

$$\omega = \mathrm{i}\,m^2 f_1(H, \mu_r, \kappa_r) + \mathrm{i}\,m^4\frac{f_3(H, \mu_r)}{Ca}. \tag{6.17}$$

Figure 10 shows the efficacy of the long-wave approach in predicting the dispersion curves compared with the numerical approach for $k < 0.2$. For $k > 0.2$, the dispersion curves predicted by both approaches start to differ such that the long-wave approach predicts a higher growth rate. This indicates that the higher-order terms missed due to the truncation of the solution to $O(\epsilon)$ terms lead to an additional stabilisation. It must be noted that one can extend the above model beyond $O(\epsilon)$ terms by following the procedure outlined by Ruyer-Quil & Manneville (1998), which could further improve the agreement between the numerical and long-wave approaches. Despite the quantitative differences in the growth rate predicted by the long-wave approach however, it does succeed in capturing the qualitative characteristics of the dispersion curve for an arbitrary wavenumber such as stabilisation due to the interface tension. Additionally, the evolution equation approach yields an equation that can be utilised to study the spatio-temporal and weakly nonlinear evolution of the flow as discussed below. Due to this, the evolution equation approach is more useful than the asymptotic approach but the latter offers a simpler mathematical treatment compared with the former.

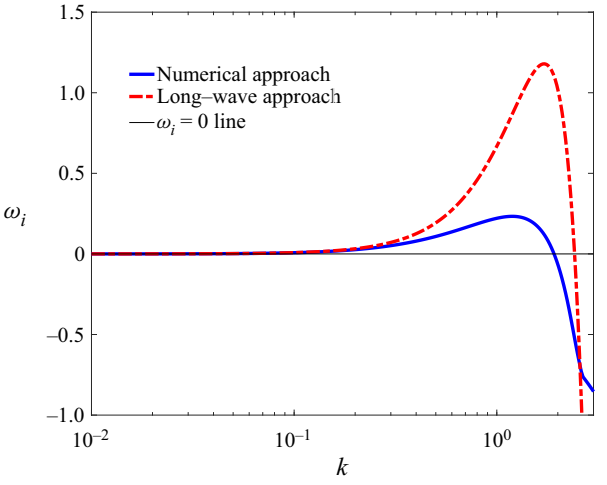

Figure 10. Comparison between the growth rate predicted by the numerical and long-wave approaches for the streamwise mode at $Re = 10, H = 0.4, \mu_r = 0.1, \kappa_r = 1, Ca = 0.1$ and $Pr = 7$. The excellent agreement between both approaches for $k < 0.2$ validates the long-wave analysis. For $k > 0.2$, the dispersion curve predicted by the long-wave analysis predicts a higher growth rate compared with the numerically obtained dispersion curve. The spanwise mode also shows a similar trend.

6.2. *Spatio-temporal stability analysis ($k_i \neq 0$)*

The GLSA in § 4 and long-wave stability studied in § 6.1 carry out the temporal stability analysis since the frequency of the disturbances, ω, is considered to be a complex number while the wavenumbers, k and m, are assumed to be real numbers (Drazin & Reid 1981). The temporal stability analysis is used to determine the evolution of the disturbances with time. Similarly, spatial stability analysis studies the evolution of disturbances in space. For the spatial stability analysis, ω is taken as a real number and k as a complex number (Drazin 2002). The spatio-temporal stability analysis predicts the evolution of the disturbances in both space and time. In this case, both ω and k are treated as complex numbers (Huerre & Monkewitz 1990; Schmid & Henningson 2001) and instability is classified as either an absolute or convective instability.

The existence of absolute instability implies the growth of disturbances in both upstream and downstream directions, while the presence of convective instability signifies that the disturbances develop only in the downstream direction from the source of the disturbances (Briggs 1964). Thus, in a convectively unstable flow, at any fixed position in space the unstable disturbances will decay if provided sufficient time (Huerre & Monkewitz 1990), resulting in mixing only in the downstream direction, while in an absolutely unstable flow, the disturbances will induce mixing both upstream and downstream. This can be illustrated by considering the response of a given base velocity profile to an impulse excitation at asymptotically long times (Huerre & Monkewitz 1990), where the obtained response is used to determine whether the flow is absolutely or convectively unstable. This section is aimed at understanding the effect of thermocapillarity and shear flow in introducing absolute instability. It must be noted that, for a system with a sustained inlet noise, the convectively unstable flow can also lead to enhancement in mixing.

To understand the absolute and convective instabilities, assume a dispersion relation of the form $\omega = \mathcal{G}(k)$, where $\mathcal{G}(k)$ is a continuous and differentiable function of k. For the absolute instability to exist, the group velocity of the disturbances must vanish for at least one value of k, so that $\partial\omega/\partial k = 0$ (Huerre & Monkewitz 1990; Schmid &

Henningson 2001). However, the determined saddle point must also obey the causality principle for the existence of the absolute instability (Huerre & Monkewitz 1990). To obtain the sufficient condition, the equation $\partial\omega/\partial k = 0$ is solved for k, which gives the saddle points of the dispersion relation. If the saddle point is of first order in the k plane (denoted by k_0) and ω_0 is the value of ω at the saddle point k_0, then a local Taylor expansion about this point gives $(\omega - \omega_0) \sim (k - k_0)^2$. This shows that the mapping from the k plane to the ω plane is characterised by angle doubling (i.e. phase doubling) provided that the saddle point is of the first order. Here, the k and ω planes refer to the $k_r - k_i$ and $\omega_r - \omega_i$ planes, respectively. If for at least one saddle point $\omega_{0i} > 0$ then the flow is absolutely unstable else convectively unstable (Huerre & Monkewitz 1990).

Following the procedure outlined above, we differentiate the dispersion relation (6.14) once with respect to k and solving the resulting equation for k yields three roots. Among the three roots, one is purely imaginary, thus, a spurious saddle point. The other two roots have an equal absolute value of k_r and k_i but k_r are of opposite signs. Thus, there is a mirror cusp point for $k_r < 0$ with the same growth rate but having a negative frequency $\omega_r < 0$. Here, we restrict ourselves to $k_r > 0$, thus, the cusp point under consideration has $\omega_r > 0$. It must be noted that both the cusp points have the same critical parameters. To illustrate, consider the saddle point and cusp point for $H = 0.4$, $\mu_r = 0.1$, $\kappa_r = 1$, $Re = 10$, $Ca = 0.01$ and $Ma = -10$. The above analysis yields three roots,

$$k_{01} = 0.533172\mathrm{i} \quad \text{corresponds to } \omega_{01} = 0.562612\mathrm{i}, \tag{6.18}$$

$$k_{02} = 0.71133 - 0.266586\mathrm{i} \quad \text{corresponds to } \omega_{02} = 1.05618 - 0.163357\mathrm{i}, \tag{6.19}$$

$$k_{03} = -0.71133 - 0.266586\mathrm{i} \quad \text{corresponds to } \omega_{03} = -1.05618 - 0.163357\mathrm{i}, \tag{6.20}$$

of which the first root (or saddle point) gives a spurious mode since the corresponding temporally unstable mode does not exist. The second root gives the correct cusp point while the third root gives the mirror cusp point. Furthermore, $\omega_{i0} < 0$, thus, a convectively unstable flow. The saddle point for arbitrary parameters is

$$k_0 = \frac{l_1 + l_2}{l_3}, \tag{6.21}$$

where

$$l_1 = 2\mathrm{i}Caf_3 3^{1/6}(3\mathrm{i} + \sqrt{3})(f_1 Ma + f_2 Re), \tag{6.22}$$

$$l_2 = 3^{1/3}(\mathrm{i} + \sqrt{3})\left[9Caf_3^2\omega_0 + \sqrt{3}\sqrt{-Ca^2f_3^3[8Ca(f_1Ma + f_2Re)^3 - 27f_3\omega_0^2]}\right]^{2/3}, \tag{6.23}$$

$$l_3 = 12f_3\left[9Caf_3^2\omega_0 + \sqrt{3}\sqrt{Ca^2f_3^3[-8Ca(f_1Ma + f_2Re)^3 + 27\omega_0^2]}\right]^{1/3}, \tag{6.24}$$

where $q = \omega_0/f_0$ has been used. The corresponding cusp point can be readily obtained by substituting $k = k_0$ in the dispersion relation (6.14). To understand the role of thermocapillarity and shear flow in causing absolute instability individually and combined, the spatio-temporal analysis results have been divided into three cases.

6.2.1. *Purely shear-flow mode ($Ma = 0$)*

This case corresponds to the case studied by Sahu & Matar (2011). The saddle point (6.24) can be readily obtained by substituting $Ma = 0$. For realistic dispersion relations, finding

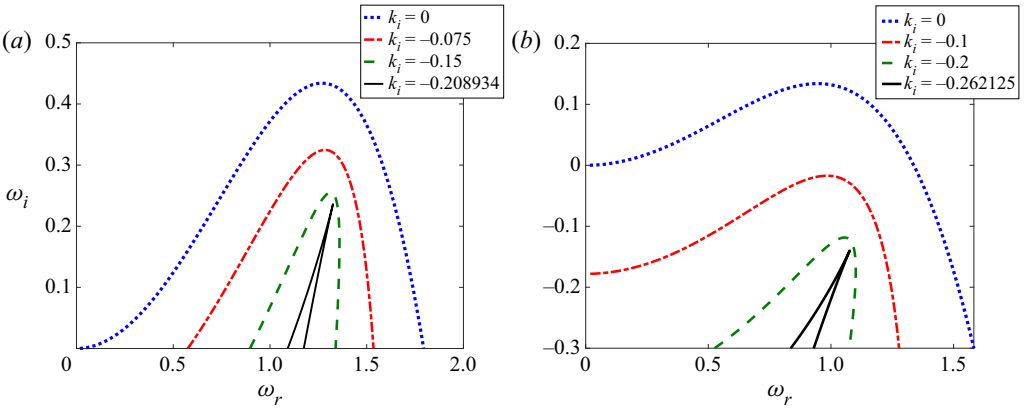

Figure 11. The existence of the (*a*) absolutely unstable flow at $Re = 45$ and (*b*) convectively unstable flow at $Re = 25$ due to the shear-flow mode of instability. The other parameters are $H = 0.4$, $\mu_r = 0.1$, $Ca = 0.01$ and $Ma = 0$. To determine the genuine character of the formed cusp point, a straight line is drawn from the cusp point and the number of times its intersections with the curve for $k_i = 0$ are counted. In both cases, such a line intersects the $k_i = 0$ curve once, thus, an odd number of times. Thus, both the cusp points are genuine. In panel (*a*), $\omega_{i0} > 0$, thus, an absolutely unstable flow, while in panel (*b*), $\omega_{i0} < 0$ implying a convectively unstable flow. (*a*) Absolutely unstable, (*b*) convectively unstable.

the saddle point in the k plane and a cusp point in the ω plane according to Briggs (1964) method becomes a cumbersome mathematical and numerical task. A simpler alternative is the method of Kupfer, Bers & Ram (1987), in which for the prediction of an absolute instability, only the formation of the cusp point in the ω plane is necessary. If the formed cusp point corresponds to $\omega_{i0} > 0$ and is genuine, then the flow is absolutely unstable. Given the relative ease of the Kupfer *et al.* (1987) method, it will be employed in the present study, to determine whether the flow is absolutely or convectively unstable.

Briefly, the Kupfer *et al.* (1987) method is as follows. First, a temporal stability curve is obtained in the ω plane by fixing $k_i = 0$ and varying k_r in the dispersion relation. Next, a negative value of k_i is fixed and k_r is varied, to obtain a curve in the ω plane. This step is repeated until a cusp point forms in the ω plane. A straight line is then drawn parallel to the ω_i axis from the cusp point extending to $\omega_i \to \infty$, which will intersect the temporal stability curve at least once. If the number of intersections with the temporal stability curve is an odd number then the formed cusp point is genuine; if the count is even then it is an evanescent cusp point. The existence of a genuine cusp point implies the presence of absolute instability, while that of an evanescent mode signifies a spurious cusp point (Yeo, Khoo & Zhao 1999, 2001; Patne & Shankar 2017; Patne & Ramon 2020).

Figure 11 illustrates the genuine cusp points in the ω plane exhibiting absolute and convectively unstable flows. Figure 11 also shows that as the Reynolds number is increased, the flow can become absolutely unstable, thus, there is a critical value of the Reynolds number, Re_a, beyond which the flow is absolutely unstable. The saddle point (6.24) and dispersion relation (6.14) are utilised to find out Re_a at which $\omega_{i0} = 0$ for varying H. The result is plotted in figure 12. For $H < 0.4$, Re_a rapidly increases with increasing H but plateaus in $0.4 < H < 0.5$ and once again starts steeply increasing for $H > 0.6$. The flow is temporally unstable for $H < 0.76$, otherwise stable such that, for $H < 0.76$, as long as $Re \neq 0$ the flow is temporally unstable, but figure 12 shows that there is a finite Re required to set in absolute instability. Consequently, for $Re < Re_a$, the temporally unstable disturbances will only grow with respect to time but will decay at any fixed position.

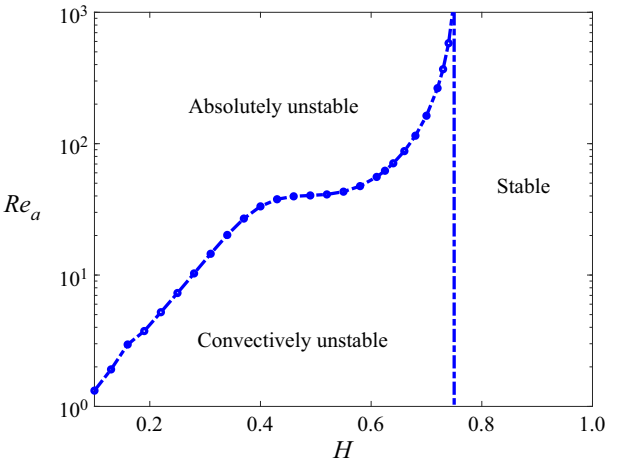

Figure 12. The variation of the critical Reynolds number for the onset of the absolute instability Re_a with H at $\mu_r = 0.1, \kappa_r = 1, Ma = 0$ and $Ca = 0.01$. The figure shows the absolutely and convectively unstable regions due to the shear-flow instability. For $H > 0.76$, the shear-flow mode is temporally stable.

However, for $Re > Re_a$, the disturbances will start growing both upstream and downstream which will lead to the enhancement of the mixing and may lead to the development of the global mode of instability (Huerre & Monkewitz 1990). A similar curve can also be obtained for $\mu_r = 10$, not shown here for brevity. By symmetry, for such a system, the shear-flow mode will be temporally unstable for $H > 0.24$ which will exhibit an absolutely unstable region for $H > 0.24$ and stable region for $H < 0.24$ with $Re_a \to \infty$ as $H \to 0.24$.

6.2.2. *Purely thermocapillary mode ($Re = 0$)*

In this case, $Re = 0$ is substituted in the dispersion relation (6.14) and the saddle point (6.24). First, consider the case with $q = 0$, i.e. the base state is a stationary two-layer system. In such a case, the thermocapillary mode of instability is a stationary mode that is inherently absolutely unstable provided that the flow is temporally unstable. Thus, the system due to pure thermocapillarity in the absence of the base-state flow becomes simultaneously temporally and absolutely unstable. Furthermore, for $q = 0$, dispersion relations for the streamwise mode (6.14) and spanwise mode (6.17) become identical, thus, both modes become unstable at the same critical parameters.

Next, consider the case with $q > 0$ but $Re = 0$ implying a creeping or stokes flow where the inertial terms in the governing equations are negligible compared with the viscous terms. In this case, the imaginary parts of the complex frequency for streamwise and spanwise modes are identical (see (6.14) and (6.17)), thus, both modes will become temporally unstable at the same critical parameters. However, the streamwise mode has a non-zero base-state flow and is thus a travelling mode while the spanwise mode is stationary. The base-state flow may lead to the existence of the convectively unstable flow due to the streamwise mode, as illustrated in figure 13(*b*). It must be noted that the streamwise mode does become absolutely unstable albeit at a higher $|Ma|$, as shown in figure 13(*a*). The spanwise mode, however, becomes absolutely and temporally unstable at identical $|Ma|$ since there is no shear flow in the spanwise direction, thereby making the flow absolutely unstable even in the presence of the shear flow. This also implies that the spanwise mode will dominate the absolute instability region for $Re = 0$.

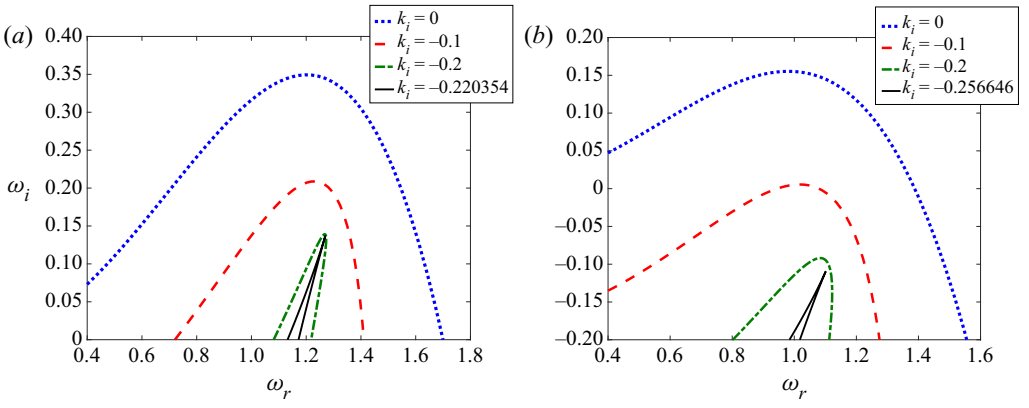

Figure 13. The existence of an (*a*) absolutely unstable flow at $Ma = -30$ and (*b*) convectively unstable flow at $Ma = -20$ due to the streamwise thermocapillary mode. The other parameters are $H = 0.4$, $\mu_r = 0.1$, $Ca = 0.01$, $\kappa_r = 1$ and $Re = 0$. The figure illustrates that the streamwise mode may become convectively or absolutely unstable due to the shear flow. (*a*) Absolutely unstable, (*b*) convectively unstable.

6.2.3. *Combined shear-flow and thermocapillary mode*

This case corresponds to the problem under consideration where we have both active shear-flow and thermocapillary modes of instability with the relevant dispersion relations (6.14) and (6.17) and saddle point (6.24). For the parametric range where the shear flow destabilises and thermocapillarity stabilises, from (6.17) the spanwise mode is stable while from (6.17) the streamwise mode is unstable, thus, only the latter can give rise to the absolute instability. However, for the streamwise mode to introduce absolute instability, it must overcome the thermocapillarity stabilisation.

For the parametric range where the thermocapillarity destabilises, the spanwise mode will lead to absolute and temporal instability at an identical $|Ma|$. Thus, for the streamwise mode to cause an absolute instability with a higher ω_{i0} at a lower $|Ma|$, the shear-flow mode must be absolutely unstable, i.e. $Re > Re_a$. A high Re implies the requirement of a higher velocity and from figure 12, $Re_a \sim O(1 - 10^3)$ which puts a restriction on the ability of the streamwise mode to introduce the absolute instability at a higher ω_{i0}. From table 1, if both thermocapillarity and shear flow have a destabilising effect and $Re > Re_a$ ($Re < Re_a$) then the streamwise (spanwise) mode will dominate the absolute instability region. If thermocapillarity has a destabilising (stabilising) effect and shear flow has a stabilising (destabilising) effect then the spanwise (streamwise) mode will dominate the absolute instability region.

6.3. *Weakly nonlinear analysis*

Unlike linear stability analysis, to study the weakly nonlinear stability analysis, we must retain the full nonlinear equation. However, working on weakly nonlinear analysis using such an equation even with MATHEMATICA software becomes a cumbersome exercise; thus, the subsequent analysis is restricted to the creeping-flow limit, i.e. $Re \to 0$. Thus, the aim of this section reduces to determine the effect of the shear flow on the weakly nonlinear evolution of the thermocapillary instability through the volumetric flow rate q. It must be noted that a two-layer plane Poiseuille flow with a purely long-wave shear-flow instability generally undergoes a supercritical bifurcation but may undergo a subcritical bifurcation for $H \sim 0.5$ (Hooper & Grimshaw 1985; Barthelet, Charru & Fabre 1995).

Parameters	Dominant absolutely unstable mode
$f_1 > 0, f_2 > 0, Ma > 0, Re > Re_a$	Streamwise mode
$f_1 > 0, f_2 > 0, Ma > 0, Re < Re_a$	Spanwise mode
$f_1 < 0, f_2 > 0, Ma > 0$	Streamwise mode
$f_1 < 0, f_2 < 0, Ma < 0$	Spanwise mode
$f_1 < 0, f_2 > 0, Ma < 0, Re > Re_a$	Streamwise mode
$f_1 < 0, f_2 > 0, Ma < 0, Re < Re_a$	Spanwise mode

Table 1. The table shows the parametric regime in which the streamwise and spanwise modes will dominate the absolutely unstable region. The conclusions can be inferred using the dispersion relations (6.14) and (6.17) for the streamwise and spanwise modes, respectively, and figure 12.

Following Cheng, Chen & Lai (2001) and Patne *et al.* (2021), we introduce slow time scales $T_1 = \xi t$, $T_2 = \xi^2 t$, where $\xi \ll 1$ is a small parameter related to the deviation of the Marangoni number Ma from its critical value Ma_c,

$$\xi^2 = \frac{Ma - Ma_c}{Ma_c}. \tag{6.25}$$

Next, we expand Ma and $h(x, t)$ into series of ξ,

$$Ma = Ma_c(1 + \xi^2), \tag{6.26a}$$

$$h(x, t) = \xi h_1(x, t, T_1, T_2) + \xi^2 h_2(x, t, T_1, T_2) + \xi^3 h_3(x, t, T_1, T_2) + \cdots, \tag{6.26b}$$

where Ma_c is the critical value of the Marangoni number obtained by solving dispersion relation (6.17) for $\omega_i = 0$ with $k = k_c = 2\pi/L$ being the cutoff wavenumber and L the length of the periodic domain,

$$f_1(H, \mu_r, \kappa_r)Ma_c + \frac{f_3(H, \mu_r)}{21}k_c^2 = 0. \tag{6.27}$$

Next, $k_c = 2\pi/L$ and Ma_c obtained in the previous step are substituted into the generalized equation (6.8*a*). The problem is then solved order by order in ξ in terms of h_i.

At $O(\delta)$, the linear stability equation is obtained with the solution of the form $h_1(x, t, T_1, T_2) = A(T_1, T_2)\exp(\mathrm{i}k_c x - \omega_r t) + \text{c.c.}$, where $A(T_1, T_2)$ is the unknown complex amplitude of the perturbation and c.c. denotes complex conjugate. It must be noted that the spanwise mode is stationary (see (6.17)), thus, for the spanwise mode, $\omega_r = 0$ in the solution while, for the streamwise mode, ω_r will be the real part of the dispersion relation (6.14). At $O(\xi^2)$, the solvability condition yields a linear differential equation in terms of the temporal growth rate of the amplitude $A(T_1, T_2)$ in the slow time scale T_1. Additionally, the solution of the differential equation at $O(\xi^2)$ is similar to h_1, such that $h_2(x, t, T_1, T_2) = B(T_1, T_2)\exp(2(\mathrm{i}k_c x - \omega t)) + \text{c.c.}$ with the complex amplitude $B(T_1, T_2)$ proportional to $A(T_1, T_2)^2$.

At $O(\xi^3)$, the Landau equation governing the weakly nonlinear temporal evolution of the amplitude function $A \equiv A(T_1, T_2)$ in slow time T_2 is obtained,

$$\partial_{T_2} A = \lambda_1 A + \lambda_2 |A|^2 A, \tag{6.28}$$

where the parameter λ_1 is concerned about the linear growth of the perturbations and will be proportional to $Ma - Ma_c$. For the spanwise mode at $\kappa_r = 1$,

$$\lambda_1 = -\frac{2}{\xi^2} CaH^3 k_c^4 (Ma - Ma_c)(1-H)^3 [1 + H(\mu_r - 1)] \\ [1 + H(\mu_r - 1)(4 - 6H + 4H^2 + H^3(\mu_r - 1))]. \tag{6.29}$$

At the onset of instability, λ_1 vanishes. The other parameter λ_2 is associated with the weakly nonlinear temporal evolution of the perturbations near the critical point. For the spanwise mode at $\kappa_r = 1$,

$$\left.\begin{aligned} \lambda_2 &= Ca(H-1)Hk_c^4 \frac{\alpha}{\beta}, \\ \alpha &= (H-1)^{10}(75 - 414H + 67H^2) \\ &\quad - 2\mu_r H(H-1)^7(299 - 1424H + 2455H^2 - 1163H^3 + 201H^4) \\ &\quad + H^2\mu_r^2(H-1)^5(-1086 + 6394H - 14433H^2 + 13839H^3 - 4415H^4 + 1005H^5) \\ &\quad - 2H^3\mu_r^3(H-1)^3(292 - 2727H + 8735H^2 - 12686H^3 + 8018H^4 - 2010H^5 + 670H^6) \\ &\quad + H^5\mu_r^4(H-1)^2(-1304 + 6410H - 10644H^2 + 6229H^3 - 610H^4 + 1005H^5) \\ &\quad - 2H^7\mu_r^5(H-1)(368 - 801H + 172H^2 + 359H^3 + 201H^4) \\ &\quad + H^{10}\mu_r^6(-272 + 280H + 67H^2), \\ \beta &= 5[1 + H(\mu_r - 1)][1 - 2H + H^2 - H^2\mu_r]^2. \end{aligned}\right\} \tag{6.30}$$

Similar expressions for λ_1 and λ_2 could also be derived for the streamwise mode. However, those will be more complicated owing to non-zero ω_r and q, thus, will not be given here.

For a stationary liquid layer on a heated substrate and other surfaces exposed to an inert gas, $\lambda_2 > 0$ (Patne *et al.* 2021) and λ_2 is a real number, thus, the layer undergoes a subcritical pitchfork bifurcation and perturbations will grow beyond the critical parameters. The present analysis for the explored parameter range shows that for a stationary two-layer system, in the absence of the shear flow (i.e. $q = 0$), subjected to a wall-normal temperature gradient both streamwise and spanwise modes exhibit a subcritical pitchfork bifurcation. For example, at $\mu_r = 2, H = 0.8, \kappa_r = 1$ and $Ca = 0.001$, $\lambda_2 = 0.00114$. However, in the presence of the shear flow (i.e. $q > 0$), λ_2 becomes a complex number, thus, the system will undergo a Hopf bifurcation. The real part of λ_2, i.e. λ_{2r}, may become negative for $q > 0$, thereby showing the existence of a supercritical Hopf bifurcation. It must be noted that q is not an independent quantity but a function of μ_r and H, *viz.*,

$$q = \frac{1 + H(\mu_r - 1)[4 - 6H + 4H^2 + H^3(\mu_r - 1)]}{6H\mu_r(H-1)} \tag{6.31}$$

obtained by integrating the base-state velocity profiles (2.6*b*) over the flow domain. To illustrate the impact of the shear flow, consider the same case at $\mu_r = 2, H = 0.8, \kappa_r = 1$ and $Ca = 0.001$ but with $q = 1.4675$, then $\lambda_2 = -5.7177 + 2.4066\mathrm{i}$ with $\lambda_{2r} < 0$ and $\lambda_{2i} \neq 0$, thus, the flow undergoes a supercritical Hopf bifurcation.

The physical consequence of the transition from a subcritical to supercritical bifurcation could be explained as follows. A stationary liquid layer on a heated substrate and other free

surface ruptures or forms dry spots due to thermocapillary instability as follows (Oron *et al.* 1997; Oron 2000). At $Ma = Ma_c$, the layer becomes linearly unstable via the process explained in § 5, thereby leading to unstable thermal perturbations. For $Ma > Ma_c$, the layer undergoes subcritical bifurcation, thus, from (6.28) the amplitude of the unstable thermal perturbations will start increasing which leads to increasing peaks and troughs in the perturbation wave. The trough eventually becomes sufficiently deep to result in the dry spot formation or rupture. As in the present case, if a shear flow is introduced then the symmetry is broken and there will be a net movement of the fluid from left to right assuming a decreasing pressure gradient. In this case, when a trough forms, the net movement of the liquid will fill that trough while decreasing the height of the peak simultaneously. This leads to the absence of the film rupture. Thus, the shear flow could hamper the film rupture and lead to a supercritical bifurcation.

7. Conclusions

In the present work we study the linear spatio-temporal stability analysis of a two-layer pressure-driven flow subjected to a wall-normal temperature gradient. The stability of the flow has been analysed using both the numerical and long-wave approaches. The analysis reveals an interesting interplay between thermocapillarity and shear flow. The thermocapillarity, arising from the temperature dependence of the interface tension, leads to thermocapillary instability while the shear flow, due to the imposed pressure gradient, leads to the shear-flow instability. The unstable modes can be further classified as streamwise and spanwise modes depending on the wavenumber under consideration. The shear flow does not contribute to the stability of the spanwise modes since the base-state flow does not affect the latter. Alvarez & Uguz (2013) predicted a negligible effect of the shear flow on the thermocapillary instability. However, the present study clearly shows that the shear flow can have a stabilising or destabilising effect on the thermocapillary mode, depending on the parameters.

The streamwise thermocapillary mode can lead to an unstable flow even if the shear-flow mode predicts a stable flow similar to a two-layer plane Couette flow subjected to a temperature gradient (Wei 2006). However, unlike two-layer plane Couette flow, depending on the values of μ_r and κ_r, there is a certain range of H for which the unstable flow due to the shear-flow mode can not be stabilised using the streamwise thermocapillary mode. The spanwise mode is stationary, unlike the travelling streamwise mode. When the shear-flow mode has a destabilising influence, the dominant mode of instability is the streamwise mode. Otherwise, the spanwise mode determines the stability of the flow.

The physical origin of the thermocapillary mode of instability has been explained using the instantaneous hot-spot generation due to thermal perturbations. For the thermocapillary instability in a liquid layer situated on a heated substrate, the hot spot that develops at the surface receives the energy for the growth only from the liquid. However, in the two-layer flow considered, both layers may provide/extract energy to/from the hot spot depending on the imposed temperature gradient, interface position, viscosity ratio and thermal conductivity ratio. Such a feat could be achieved by the upflow and downflow that develop in fluids 1 and 2, respectively.

As the interface position (i.e. H) approaches the plate with a higher temperature, the thermocapillary mode becomes unstable due to the increasing capability of the corresponding flow to heat the hot spot. While a decreasing κ_r leads to an increasingly unstable flow due to the diffusion-mediated energy gain by the flow from the hotter fluid side and the opposite from the colder fluid side. For $\mu_2 \gg \mu_1$, the dynamics of fluid 1 could be ignored, and the opposite is true for $\mu_2 \ll \mu_1$.

The evolution equation for the flow in the long-wave limit is derived, which is then utilised to analyse the linear spatio-temporal and weakly nonlinear stability analysis. The dispersion curves obtained using the pseudo-spectral numerical method and the long-wave evolution equation show good agreement for $k < 0.2$. The spatio-temporal stability analysis predicts an absolutely unstable flow due to the shear-flow mode, even without thermocapillarity. When the pressure gradient is switched off, then the two-layer system can still exhibit absolute instability due to both streamwise and spanwise thermocapillary modes arising because of the imposed temperature gradient at the same parameters. Also, when $Re > Re_a$ ($Re < Re_a$) and thermocapillarity has a destabilising effect, then the streamwise (spanwise) mode will dominate the absolute instability region.

The weakly nonlinear analysis shows that without a shear flow, the two-layer system subjected to a wall-normal temperature gradient will undergo a subcritical pitchfork bifurcation simultaneously through the streamwise and spanwise modes. However, as soon as the shear flow is switched on, the streamwise mode undergoes a supercritical Hopf bifurcation. The physical manifestation of this change in the type of bifurcation has been discussed.

The present study thus shows that the stability of a two-layer pressure-driven flow subjected to a wall-normal temperature gradient strongly depends on the interface position, imposed temperature gradient sign, and viscosities and thermal conductivities of the fluids. The present study could be further extended to the fully nonlinear regime using the derived evolution equation, which could further reveal the interplay between the pressure and temperature gradients that could help in practical applications to control undesirable patterns. Also, the present study considers Newtonian fluids. However, additive manufacturing and polymer co-extrusion processes involve non-Newtonian fluids. Thus, the present study could be extended to include the non-Newtonian behaviour of the fluids.

Funding. The author acknowledges financial support from the Indian Institute of Technology Hyderabad, India under grant no. SG/IITH/F280/2022-23/SG-118.

Declaration of interests. The authors report no conflict of interest.

Author ORCIDs.
Ramkarn Patne https://orcid.org/0000-0003-4052-1807.

References

Alvarez, N.J. & Uguz, A.K. 2013 The impact of deformable interfaces and Poiseuille flow on the thermocapillary instability of three immiscible phases confined in a channel. *Phys. Fluids* **25**, 024104.

Barmak, I., Gelfgat, A., Vitoshkin, H., Ullmann, A. & Brauner, N. 1994 Stability of stratified two-phase flows in horizontal channels. *Phys. Fluids* **28**, 044101.

Barthelet, P., Charru, F. & Fabre, J. 1995 Experimental study of interfacial long waves in a two-layer shear flow. *J. Fluid Mech.* **303**, 23–53.

Bird, R.B., Armstrong, R.C. & Hassager, O. 1977 *Dynamics of Polymeric liquids*, vol. 2. Wiley.

Boomkamp, P.A.M., Boersma, B.J., Miesen, R.H.M. & Beijnon, G.V. 1997 A Chebyshev collocation method for solving two-phase flow stability problems. *J. Comput. Phys.* **132**, 191–200.

Bretherton, F.P. 1961 The motion of long bubbles in tubes. *J. Fluid Mech.* **10**, 166–188.

Briggs, R.J. 1964 *Electron-Stream Interaction with Plasmas*. MIT.

Charru, F. & Hinch, E.J. 2000 'Phase diagram' of interfacial instabilities in a two-layer Couette flow and mechanism of the long-wave instability. *J. Fluid Mech.* **414**, 195–223.

Cheng, P.J., Chen, C.K. & Lai, H.Y. 2001 Nonlinear stability analysis of thin viscoelastic film flow traveling down along a vertical cylinder. *Nonlinear Dyn.* **24**, 305–332.

Chua, C.K. & Leong, K.F. 2017 *3D Printing and Additive Manufacturing: Principles and Applications. In Fifth Edition of Rapid Prototyping*, 5th edn. World Scientific.

DE SAEDELEER, C., GARCIMARTIN, A., CHAVEPEYER, G., PLATTEN, J.K. & LEBON, G. 1996 The instability of a liquid layer heated from the side when the upper surface is open to air. *Phys. Fluids* **8**, 670–676.

DRAZIN, P.G. 2002 *Introduction to Hydrodynamic Stability*. Cambridge University Press.

DRAZIN, P.G. & REID, W.H. 1981 *Hydrodynamic Stability*. Cambridge University Press.

EZERSKY, A.B., GARCIMARTIN, A., MANCINI, H.L. & PEREZ-GARCIA, C. 1993 Spatiotemporal structure of hydrothermal waves in Marangoni convection. *Phys. Rev.* E **48**, 4414–4422.

GEORIS, P., HENNENBERG, M., LEBON, G. & LEGROS, J.C. 1999 Investigation of thermocapillary convection in a three-liquid-layer system. *J. Fluid Mech.* **389**, 209–228.

GEORIS, P., HENNENBERG, M., SIMANOVSKII, I.B., NEPOMNYASHCHY, A.A., WERTGEIM, I.I. & LEGROS, J.C. 1993 Thermocapillary convection in a multilayer system. *Phys. Fluids* A **5** (7), 1575–1582.

GIBSON, I., ROSEN, D.W. & STUCKER, B. 2010 *Additive Manufacturing Technologies*. Springer.

GOH, G.D., YAP, Y.L., AGARWALA, S. & YEONG, W.Y. 2018 Recent progress in additive manufacturing of fiber reinforced polymer composite. *Adv. Mater. Technol.* **4**, 1800271.

HINCH, E.J. 1984 A note on the mechanism of the instability at the interface between two shearing fluids. *J. Fluid Mech.* **144**, 463–465.

HOOPER, A.P. & GRIMSHAW, R. 1985 Nonlinear instability at the interface between two viscous fluids. *Phys. Fluids* **28**, 37–45.

HUERRE, P. & MONKEWITZ, P.A. 1990 Local and global instabilities in spatially developing flows. *Annu. Rev. Fluid Mech.* **22**, 173–537.

JOSEPH, D.D., BAI, R., CHEN, K.P. & RENARDY, Y.Y. 1997 Core-annular flows. *Annu. Rev. Fluid Mech.* **29**, 65–90.

JOSEPH, D.D. & RENARDY, Y.Y. 1993 *Fundamentals of Two-Fluid Dynamics : Part 1, Mathematical Theory and Applications*. Springer.

KISTLER, S.F. & SCHWEIZER, P.M. 1997 *Liquid Film Coating: Scientific Principles and Their Technological Implications*. Springer.

KUPFER, K., BERS, A. & RAM, A.K. 1987 The cusp map in complex-frequency plane for absolute instabilities. *Phys. Fluids* **30**, 3075–3082.

LAPPA, M. 2010 *Thermal Convection: Patterns, Evolution and Stability*. Wiley.

LEVENSPIEL, O. 1999 *Chemical Reaction Engineering*. Wiley.

LI, M., XU, S. & KUMACHEVA, E. 2000 Convection in polymeric fluids subjected to vertical temperature gradients. *Macromolecules* **33**, 4972–4978.

MADRUGA, S., PÉREZ-GARCIA, C. & LEBON, G. 2003 Convective instabilities in two superposed horizontal liquid layers heated laterally. *Phys. Rev.* E **68**, 041607.

MADRUGA, S., PÉREZ-GARCIA, C. & LEBON, G. 2004 Instabilities in two-liquid layers subject to a horizontal temperature gradient. *Theor. Comput. Fluid Dyn.* **18**, 277–284.

MIZEV, A.I. & SCHWABE, D. 2009 Convective instabilities in liquid layers with free upper surface under the action of an inclined temperature gradient. *Phys. Fluids* **21**, 112102.

NEPOMNYASHCHY, A.A. & SIMANOVSKII, I.B. 2006 Convective flows in a two-layer system with a temperature gradient along the interface. *Phys. Fluids* **18**, 032105.

ORON, A. 2000 Nonlinear dynamics of irradiated thin volatile liquid films. *Phys. Fluids* **12**, 29–41.

ORON, A., DAVIS, S.H. & BANKOFF, S.G. 1997 Long-scale evolution of thin liquid films. *Rev. Mod. Phys.* **69**, 931–980.

OSPENNIKOV, N.A. & SCHWABE, D. 2004 Thermocapillary flow without return flow-linear flow. *Exp. Fluids* **36**, 938–945.

PATNE, R., AGNON, Y. & ORON, A. 2020 Marangoni instability in the linear Jeffreys fluid with a deformable surface. *Phys. Rev. Fluids* **5**, 084005.

PATNE, R., AGNON, Y. & ORON, A. 2021 Thermocapillary instabilities in a liquid layer subjected to an oblique temperature gradient. *J. Fluid Mech.* **906**, A12.

PATNE, R., AGNON, Y., ORON, A. & RAMON, G. 2022 Dynamics of a two-layer flow with a heat source/sink along the interface: viscosity stratification. *J. Fluid Mech.* **934**, A43.

PATNE, R. & RAMON, G.Z. 2020 Stability of fluid flows coupled by a deformable solid layer. *J. Fluid Mech.* **905**, A36.

PATNE, R. & SHANKAR, V. 2017 Absolute and convective instability in combined Couette-Poiseuille flow past a neo-Hookean solid. *Phys. Fluids* **29**, 124104.

PEARSON, J.R.A. 1958 On convection cells induced by surface tension. *J. Fluid Mech.* **4**, 489–500.

QUAN, Z., WU, A., KEEFE, M., QIN, X., YU, J., SUHR, J., BYUN, J.-H., KIM, B.-S. & CHOU, T.-W. 2015 Additive manufacturing of multi-directional preforms for composites: opportunities and challenges. *Mater. Today* **18**, 503–512.

RAJAK, D.K., PAGAR, D.D., MENEZES, P.L. & LINUL, E. 2019 Fiber-reinforced polymer composites: manufacturing, properties, and applications. *Polymers* **11** (10), 1667.

RUYER-QUIL, C. & MANNEVILLE, P. 1998 Modeling film flows down inclined planes. *Eur. Phys. J.* B **6**, 277–292.

SAHU, K.C. & MATAR, O.K. 2011 Three-dimensional convective and absolute instabilities in pressure-driven two-layer channel flow. *Intl J. Numer. Meth. Fluids* **37**, 987–93.

SAMANTA, A. 2013 Effect of surfactant on two-layer channel flow. *J. Fluid Mech.* **735**, 519–552.

SCHATZ, M.F. & NEITZEL, G.P. 2001 Experiments on thermocapillary instabilities. *Annu. Rev. Fluid Mech.* **33**, 93–127.

SCHMID, P.J. & HENNINGSON, D.S. 2001 *Stability and Transition in Shear Flows*. Springer.

SIMANOVSKII, I.B. 2007 Nonlinear buoyant-thermocapillary flows in a three-layer system with a temperature gradient along the interfaces. *Phys. Fluids* **19**, 082106.

SMITH, M.K. 1990 The mechanism for the long-wave instability in thin liquid films. *J. Fluid Mech.* **217**, 469–485.

SMITH, M.K. & DAVIS, S.H. 1983*a* Instabilities of dynamic thermocapillary liquid layers. Part 1. Convective instabilities. *J. Fluid Mech.* **132**, 119–144.

SMITH, M.K. & DAVIS, S.H. 1983*b* Instabilities of dynamic thermocapillary liquid layers. Part 2. Surface-wave instabilities. *J. Fluid Mech.* **132**, 145–162.

TILLEY, B.S., DAVIS, S.H. & BANKOFF, S.G. 1994 Linear stability theory of two-layer fluid flow in an inclined channel. *Phys. Fluids* **6**, 3906.

TREFETHEN, L.N. 2000 *Spectral Methods in MATLAB*. SIAM.

WEI, H.H. 2006 Shear-flow and thermocapillary interfacial instabilities in a two-layer viscous flow. *Phys. Fluids* **18**, 064109.

YEO, K.S., KHOO, B.C. & ZHAO, H.Z. 1999 The convective and absolute instability of fluid flow over viscoelastic compliant layers. *J. Sound Vib.* **223** (3), 379–398.

YEO, K.S., KHOO, B.C. & ZHAO, H.Z. 2001 Turbulent boundary layer over a compliant surface: absolute and convective instabilities. *J. Fluid Mech.* **449**, 141–168.

YIANTSIOS, S.G. & HIGGINS, B.G. 1988 Linear stability of plane poiseuille flow of two superposed fluids. *Phys. Fluids* **31**, 3225–3238.

YIH, C.-S. 1967 Instability due to viscosity stratification. *J. Fluid Mech.* **27**, 337–350.